

Excitation functions of related parameters from transverse momentum (mass) spectra in high energy collisions

Li-Li Li¹, Fu-Hu Liu^{1,*}, Muhammad Waqas¹, Rasha Al-Yusufi^{1,2}, Altaf Mujear^{1,2}

¹*Institute of Theoretical Physics and State Key Laboratory of Quantum Optics and Quantum Optics Devices, Shanxi University, Taiyuan, Shanxi 030006, China*

²*Physics Department, Faculty of Science, Sana'a University, P. O. Box 13499, Sana'a, Republic of Yemen*

Abstract: Transverse momentum (mass) spectra of positively and negatively charged pions, positively and negatively charged kaons, protons and antiprotons produced at mid-(pseudo)rapidity in various collisions at high energies are analyzed in this work. The experimental data measured in central gold-gold, central lead-lead, and inelastic proton-proton collisions by several international collaborations are studied. The (two-component) standard distribution is used to fit the data and extract the excitation function of effective temperature. Then, the excitation functions of kinetic freeze-out temperature, transverse flow velocity, and initial temperature are obtained. In the considered collisions, the four parameters increase with the increase of collision energy in general, and the kinetic freeze-out temperature appears the trend of saturation at the top Relativistic Heavy Ion Collider and the Large Hadron Collider.

Keywords: Excitation functions of related parameters, kinetic freeze-out temperature, transverse flow velocity, initial temperature

PACS: 12.40.Ee, 13.85.Hd, 24.10.Pa

1 Introduction

It is believed that the environment of high temperature and high density is formed in the system evolution process of central nucleus-nucleus (AA) collisions at high energy [1, 2, 3], in which quark-gluon plasma (QGP) is possibly created and many particles are produced [4, 5, 6]. At present, it is impossible to detect directly the system evolution process of collisions due to very short time interval. Instead, the particle spectra at the stage of kinetic freeze-out can be measured in experiments and the mechanisms of system evolutions and particle productions can be studied indirectly [7, 8, 9], though the particle ratios reflect the property at the stage of chemical freeze-out. As for peripheral AA collisions and small collision system, the situation is similar if the multiplicity is high enough due to small system also appears collective behavior [10, 11].

Although there are different stages in the system evolution [1, 2, 3], the initial state is the most important due to its determining effect to the system evolution. In addition, chemical and kinetic freeze-outs are two im-

portant stages in the system evolution. At the stage of chemical freeze-out, the system had happened the phase transition from QGP to hadronic matter, and the constituents and ratios of various particles do not change anymore. At the stage of kinetic freeze-out, the collisions among various particles are elastic, and the transverse momentum spectra of various particles are fixed [2, 7]. In small system with low multiplicity, QGP is not expected to create in it due to a very small volume of the violent collision region. From the similar multiplicity at the energy up to 200 GeV, small system is more similar to peripheral AA collisions, but not to central AA collisions [12, 13]. At the energy down to 10 or several GeV, the situation is different due to the fact that baryon-dominated effect plays more important role in AA collisions [14].

The temperatures at the stages of kinetic freeze-out, chemical freeze-out, and initial state are called the kinetic freeze-out temperature (T_0 or T_{kin}), chemical freeze-out temperature (T_{ch}), and initial temperature (T_i), respectively. Besides, one also has the effective

*E-mail: fuhuliu@163.com; fuhuliu@sxu.edu.cn

temperature (T) in which both the contributions of thermal motion and flow effect are included. It is expected that various temperatures can be extracted from particle spectra, which are usually model dependent. Generally, T is unavoidably model dependent, and T_{ch} extracted from particle ratios in the statistical thermal model [15, 16, 17, 18] is also model dependent. We hope to use a less model dependent method to extract T_0 , β_T , and T_i . The quantities used in the method are expected to relate to experimental data as much as possible, though they can be calculated from models in some cases.

To perform a less model dependent method, we would like to use the standard distribution or its two-component form to obtain T by fitting the experimental transverse momentum (p_T) or transverse mass (m_T) spectra of various particles. The standard distribution includes the Bose-Einstein, Fermi-Dirac, and Boltzmann distributions, in which the effective temperature parameter T are the closest to that in the ideal gas model when comparing T with those in other distributions. After the fitting, we hope to extract T_0 and β_T from the relation to average p_T ($\langle p_T \rangle$) due to the Erlang distribution in multisource thermal model [19, 20, 21] and T_i from the relation to root-mean-square p_T ($\sqrt{\langle p_T^2 \rangle}$) due to the color string percolation model [22, 23, 24]. Obviously, $\langle p_T \rangle$ and $\sqrt{\langle p_T^2 \rangle}$ depend on the data themselves, though they can be calculated from models.

In this work, the p_T (m_T) spectra of positively and negatively charged pions (π^+ and π^-), positively and negatively charged kaons (K^+ and K^-), protons and antiprotons (p and \bar{p}) produced at mid-(pseudo)rapidity (mid- y or mid- η) measured in central gold-gold (Au-Au) collisions at the Alternating Gradient Synchrotron (AGS) by the E866 [25], E895 [26, 27], and E802 [28, 29] Collaborations and at the Relativistic Heavy Ion Collider (RHIC) by the STAR [30, 31, 32] and PHENIX [33, 34] Collaborations, in central lead-lead (Pb-Pb) collisions at the Super Proton Synchrotron (SPS) by the NA49 Collaboration [35, 36, 37] and at the Large Hadron Collider (LHC) by the ALICE Collaboration [38], as well as in inelastic (INEL) proton-proton (pp) collisions at the SPS by the NA61/SHINE Collaboration [39, 40], at the RHIC by the PHENIX Collaboration [41], and at the LHC by the CMS Collaboration [42, 43] are studied. The (two-component) standard distribution is used to fit the data and to extract T , T_i , T_0 , and β_T , as well as the excitation functions

(energy dependences) of parameters.

The remainder of this paper is structured as follows. The formalism and method are shortly described in Section 2. Results and discussion are given in Section 3. In Section 4, we summarize our main observations and conclusions.

2 Formalism and method

In high energy collisions, the soft excitation and hard scattering processes are two main processes of particle productions. Most light flavor particles are produced in the soft excitation process and distribute in a narrow p_T range which is less than $2 \sim 3$ GeV/ c or a little more. Some light flavor particles are produced in the hard scattering process and distribute in a wide p_T range. In collisions at not too high energies, the contribution of hard scattering process can be neglected and the main contributor to produced particles is the soft excitation process. In collisions at high energy, the contribution of hard scattering process cannot be neglected, though the main contributor to produced particles is also the soft excitation process. It is expected that the contribution fraction of hard scattering process increases with the increase of collisions energy.

The contributions of soft excitation and hard scattering processes can be described by similar or different probability density functions. Generally, the hard scattering process does not contribute mainly to the temperature and flow velocity due to its small fraction in a narrow p_T range. We can neglect the contribution of hard scattering process if we study the spectra in a not too wide p_T range. On the contribution of soft excitation process, we have more than one functions to describe the p_T spectra. These functions include, but are not limited to, the standard distribution [44], the Tsallis statistics [44, 45, 46, 47], the Erlang distribution [19, 20, 21], the Schwinger mechanism [48, 49, 50, 51], the blast-wave model with Boltzmann statistics [52, 53], the blast-wave model with Tsallis statistics [54, 55, 56], the Hagedorn thermal distribution [57], and their superposition with two- or three-component. These functions also describe partly the p_T spectra of hard scattering process in most cases.

In our opinion, in the case of fitting the data with acceptable representations, various distributions show similar behaviors which result in similar $\langle p_T \rangle$ ($\sqrt{\langle p_T^2 \rangle}$) with different parameters. To be the closest to the tem-

perature concept in the ideal gas model, we choose the standard distribution in which the chemical potential μ and spin property S are included. That is, one has the probability density function in terms of p_T to be [44]

$$f_{p_T}(p_T, T) = \frac{1}{N} \frac{dN}{dp_T} = C p_T m_T \int_{y_{\min}}^{y_{\max}} \cosh y \times \left[\exp \left(\frac{m_T \cosh y - \mu}{T} \right) + S \right]^{-1} dy, \quad (1)$$

where

$$m_T = \sqrt{p_T^2 + m_0^2}, \quad (2)$$

m_0 is the rest mass, N denotes the particle number, y_{\min} (y_{\max}) is the minimum (maximum) value in the rapidity interval, $S = -1$ ($+1$) is for bosons (fermions), and C is the normalization constant. Similarly, the probability density function in terms of m_T is

$$f_{m_T}(m_T, T) = \frac{1}{N} \frac{dN}{dm_T} = C m_T^2 \int_{y_{\min}}^{y_{\max}} \cosh y \times \left[\exp \left(\frac{m_T \cosh y - \mu}{T} \right) + S \right]^{-1} dy. \quad (3)$$

In some cases, the independent variable m_T in Eq. (3) is replaced by $m_T - m_0$ which starts at 0. Both m_T and $m_T - m_0$ show the same distribution shape. As probability density functions, the integrals of Eqs. (1) and (3) are naturally normalized to 1 respectively.

The chemical potential μ in Eqs. (1) and (3) is particle dependent. For the particle type i ($i = \pi, K$, and p in this work), its chemical potential μ_i is expressed by [34, 58, 59]

$$\mu_i = -\frac{1}{2} T_{ch} \ln(k_i), \quad (4)$$

where k_i denotes the ratio of negative to positive particle numbers,

$$T_{ch} = \frac{T_{\lim}}{1 + \exp[2.60 - \ln(\sqrt{s_{NN}})/0.45]} \quad (5)$$

is empirically the chemical freeze-out temperature in the statistical thermal model [15, 16, 17, 18], $T_{\lim} = 0.158$ GeV is the limiting or saturation temperature [3], and $\sqrt{s_{NN}}$ is the center-of-mass energy per nucleon pair in the units of GeV.

Generally, one needs one or two standard distributions to fit the p_T (m_T) spectra in a narrow range. In particular, if the resonance decays contribute a large fraction, a two-component distribution is indeed needed.

Or, if the hard scattering process contributes a sizable fraction in the considered p_T (m_T) range, a two-component distribution is also needed. In the case of using the two-component standard distribution in which the contributions from resonance decay are naturally included in the first component which covers the spectra in low- p_T region ($< 0.2 \sim 0.3$ GeV/ c), one has the probability density functions of p_T and m_T to be

$$f_{p_T}(p_T) = k f_{p_T}(p_T, T_1) + (1 - k) f_{p_T}(p_T, T_2) \quad (6)$$

and

$$f_{m_T}(m_T) = k f_{m_T}(m_T, T_1) + (1 - k) f_{m_T}(m_T, T_2) \quad (7)$$

respectively, where k denotes the contribution fraction of the first component, and $f_{p_T}(p_T, T_1)$ [$f_{p_T}(p_T, T_2)$] and $f_{m_T}(m_T, T_1)$ [$f_{m_T}(m_T, T_2)$] are given in Eqs. (1) and (3) respectively. The integrals of Eqs. (6) and (7) are also normalized to 1 respectively. Correspondingly,

$$T = k T_1 + (1 - k) T_2 \quad (8)$$

is averaged by weighting the two fractions. The temperature T defined in Eq. (8) reflects the common effective temperature of the two components in the case of the two components are assumed to stay in equilibrium.

According to the Hagedorn model [57], one may also use the usual step function $\theta(x)$ to superpose the two standard distributions, where $\theta(x) = 0$ if $x < 0$ and $\theta(x) = 1$ if $x \geq 0$. Thus, we have new probability density functions of p_T and m_T to be

$$f_{p_T}(p_T) = A_1 \theta(p_1 - p_T) f_{p_T}(p_T, T_1) + A_2 \theta(p_T - p_1) f_{p_T}(p_T, T_2) \quad (9)$$

and

$$f_{m_T}(m_T) = A_1 \theta(m_1 - m_T) f_{m_T}(m_T, T_1) + A_2 \theta(m_T - m_1) f_{m_T}(m_T, T_2) \quad (10)$$

respectively, where A_1 and A_2 are constants which result in the two components to be equal to each other at $p_T = p_1$ and $m_T = m_1$. The integrals of Eqs. (9) and (10) should be normalized to 1 respectively due to the fact that they are probability density functions. The contribution fractions of the first component in Eqs. (9) and (10) are

$$k = \int_0^{p_1} A_1 f_{p_T}(p_T, T_1) dp_T = 1 - \int_{p_1}^{p_T^{\max}} A_2 f_{p_T}(p_T, T_2) dp_T \quad (11)$$

and

$$k = \int_{m_0}^{m_1} A_1 f_{m_T}(m_T, T_1) dm_T$$

$$= 1 - \int_{m_1}^{m_T \max} A_2 f_{m_T}(m_T, T_2) dm_T \quad (12)$$

respectively, where $p_T \max$ and $m_T \max$ denote the maximum p_T and m_T respectively. Eq. (8) is also suitable for the superposition in terms of the Hagedorn model [57].

The two superpositions show respective advantages and disadvantages. The first superposition can fit the data by a smooth curve. However, there are correlations in determining T_1 and T_2 . The second superposition can determine T_1 and T_2 without correlations. However, the curves are possibly not smooth at p_1 or m_1 . In the case of obtaining $\langle p_T \rangle$ and $\sqrt{\langle p_T^2 \rangle}$, it does not matter which superposition is used, though the two T are slightly different. In this work, we use the first superposition to obtain smooth curves. One has

$$\langle p_T \rangle = \int_0^{p_T \max} p_T f_{p_T}(p_T) dp_T \quad (13)$$

and

$$\sqrt{\langle p_T^2 \rangle} = \sqrt{\int_0^{p_T \max} p_T^2 f_{p_T}(p_T) dp_T} \quad (14)$$

due to

$$\int_0^{p_T \max} f_{p_T}(p_T) dp_T = 1. \quad (15)$$

Based on m_T spectrum, we may use the same parameters to obtain $\langle p_T \rangle$ and $\sqrt{\langle p_T^2 \rangle}$ from the related formula of p_T distribution.

It should be noted that, since we aim to extract the parameters in a less model dependent way, we shall obtain $\langle p_T \rangle$ and $\sqrt{\langle p_T^2 \rangle}$ from the combination of data points and fit function in this paper. In fact, we may divide p_T (m_T) spectrum into two or three regions according to the measured and un-measured p_T (m_T) ranges. To obtain $\langle p_T \rangle$ and $\sqrt{\langle p_T^2 \rangle}$, we may use the data points in the measured p_T (m_T) range and only use the fit function to extrapolate to the un-measured p_T (m_T) range.

In each nucleon-nucleon collision in AA and pp collisions, the projectile and target participant sources contribute equally to $\langle p_T \rangle$. In the framework of multisource thermal model [19, 20, 21], each projectile and target source contribute a fraction of 1/2 to $\langle p_T \rangle$, i.e. $\langle p_T \rangle/2$ which is contributed together by the thermal motion

and flow effect. Let k_0 ($1 - k_0$) denote the contribution fraction of thermal motion (flow effect), we define empirically

$$T_0 \equiv \frac{k_0 \langle p_T \rangle}{2} \quad (16)$$

and

$$\beta_T \equiv \frac{(1 - k_0) \langle p_T \rangle}{2m_0 \bar{\gamma}}, \quad (17)$$

where $\bar{\gamma}$ is the mean Lorentz factor of the considered particles and

$$k_0 = 0.30 - 0.01 \ln(\sqrt{s_{NN}}) \quad (18)$$

is a parameterized representation in this paper due to our comparison with the results [12, 13] from the blast-wave model [52, 53, 54, 55, 56]. In Eq. (18), $\sqrt{s_{NN}}$ is in the units of GeV as that in Eq. (5).

In a recent work [60], it is shown that the effective temperature is proportional to $\langle p_T \rangle$ and the kinetic freeze-out temperature is proportional to the effective temperature, though the effective temperature used in ref. [60] is different from this paper. This confirms the relation of $T_0 \propto \langle p_T \rangle$ (Eq. (16)) used in this paper. Considering each projectile and target source contributing $\langle p_T \rangle/2$ [19, 20, 21], we have concretely $T_0 \propto \langle p_T \rangle/2$. The remainder in $\langle p_T \rangle/2$ is naturally contributed by transverse flow. This confirms Eqs. (16) and (17) to be justified, though k_0 is an empirical representation.

To continue this work, we need some assumptions and a coordinate system. In the source rest frame, the particles are assumed to emit isotropically. Meanwhile, the interactions among various sources are neglected, which affects slightly the p_T (m_T) spectra, though which affects largely anisotropic flows [61]. A right-handed coordinate system $O-xyz$ is established in the source rest frame, where Oz axis is along the beam direction, xOy plane is the transverse plane, and xOz plane is the reaction plane.

We can obtain $\bar{\gamma}$ by a Monte Carlo (MC) method. Let $R_{1,2,3}$ denote random number distributed evenly in $[0, 1]$, each concrete p_T satisfies

$$\int_0^{p_T} f_{p_T}(p'_T, T) dp'_T < R_1 < \int_0^{p_T + \delta p_T} f_{p_T}(p'_T, T) dp'_T, \quad (19)$$

where δp_T denotes a small shift relative to p_T . Each concrete emission angle θ satisfies

$$\theta = 2 \arcsin \sqrt{R_2} \quad (20)$$

due to the fact that θ obeys the probability density function $f_\theta(\theta) = (1/2)\sin\theta$ in $[0, \pi]$ in the case of isotropic assumption in the source rest frame. The solution of the equation $\int_0^\theta f_{\theta'}(\theta')d\theta' = R_2$ is Eq. (20). We give up to use rapidity due to the fact that it is unnecessary here. Each concrete momentum p , energy E , and Lorentz factor γ can be obtained by

$$p = p_T \csc \theta, \quad (21)$$

$$E = \sqrt{p^2 + m_0^2} \quad (22)$$

and

$$\gamma = \frac{E}{m_0}, \quad (23)$$

respectively. After multiple repeating calculations due to the MC method, we have

$$\bar{\gamma} = \frac{\bar{E}}{m_0}, \quad (24)$$

where \bar{E} denotes the mean E for a given type of particle.

In addition, each concrete azimuthal angle ϕ satisfies

$$\phi = 2\pi R_3 \quad (25)$$

due to the fact that ϕ obeys the probability density function $f_\phi(\phi) = 1/(2\pi)$ in $[0, 2\pi]$ in the case of isotropic assumption in the source rest frame. The solution of the equation $\int_0^\phi f_{\phi'}(\phi')d\phi' = R_3$ is Eq. (25). Each concrete momentum components p_x , p_y , and p_z can be obtained by

$$p_x = p_T \cos \phi, \quad (26)$$

$$p_y = p_T \sin \phi, \quad (27)$$

and

$$p_z = p_T \cot \theta = p \cos \theta, \quad (28)$$

respectively. By using the components and E , p , and θ , we can obtain other quantities such as (pseudo)rapidity and event structure [61] which are beyond the focus of this work and will not be studied anymore.

According to the color string percolation model [22, 23, 24], one has

$$T_i \equiv \sqrt{\frac{\langle p_T^2 \rangle}{2}}. \quad (29)$$

Meanwhile, we have the relation between the three components p_x , p_y , and p_z of the momentum p to be

$$\sqrt{\langle p_x^2 \rangle} = \sqrt{\langle p_y^2 \rangle} = \sqrt{\langle p_z^2 \rangle} = \sqrt{\frac{\langle p_T^2 \rangle}{2}}, \quad (30)$$

in which the root-mean-square components $\sqrt{\langle p_x^2 \rangle}$, $\sqrt{\langle p_y^2 \rangle}$, and $\sqrt{\langle p_z^2 \rangle}$ are used. Naturally, T_i can be given by one of the root-mean-square components.

We would like to point out that the above isotropic assumption is only performed in the source rest frame. It is expected that many sources are formed in high energy collisions according to the multisource model [19, 20, 21]. These sources distribute at different rapidities in the rapidity space, which appear the effect of longitudinal flow. The two-component p_T and m_T spectra render that these sources stay in two different excitation states or have two different decay mechanisms. The interactions among these sources also affect anisotropic flows in transverse plane [61].

3 Results and discussion

Figures 1(a)–1(q) show the p_T ($m_T - m_0$) spectra, $(1/2\pi p_T) \cdot d^2N/dydp_T$ [$(1/2\pi m_T) \cdot d^2N/dydm_T$], of π^+ , π^- , K^+ , K^- , p , and \bar{p} produced at mid- y or mid- η in central Au-Au collisions at different $\sqrt{s_{NN}}$, where the particle types, y or η intervals, centrality classes, and collision energies are marked in the panels. The closed and open symbols represent respectively the experimental data of positively and negatively charged particles measured by the E866 [25], E895 [26, 27], E802 [28, 29], STAR [30, 31, 32], and PHENIX [33, 34] Collaborations marked in the panels, where in Figs. 1(a)–1(d) the data for π^\pm and K^+ are taken from the E866 Collaboration [25] and the data for p are taken from the E895 Collaboration [26, 27]. The solid and dashed curves are our results fitted by Eq. (6) or (7) for positively and negatively charged particles respectively. The values of free parameters (T_1 , T_2 if available, k), derived parameter (T), normalization constant (N_0), χ^2 , and degree-of-freedom (dof) are listed in Table 1. The dot-dashed curves are our results fitted by using the single component function with the weighted average parameter $\langle T \rangle$ which will be discussed later. The dotted curves and asterisks in Figs. 1(a)–1(f) represent the MC results for K^+ with high (10^6 particles) and low (10^4 particles) statistics respectively, which will be discussed at the end of this section. In the fitting process for the solid and

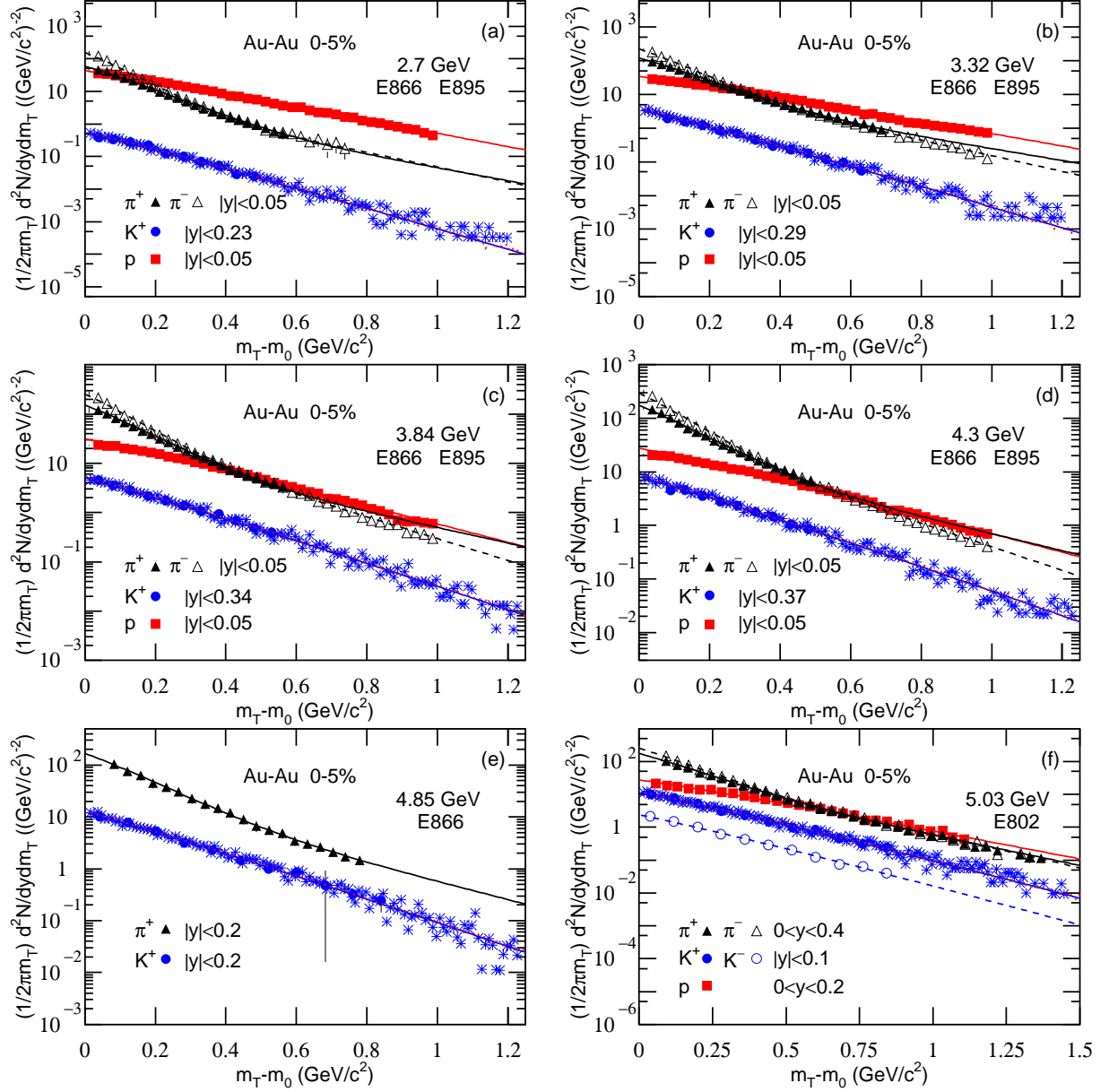


Fig. 1. The p_T ($m_T - m_0$) spectra, $(1/2\pi p_T) \cdot d^2N/dydp_T$ [$(1/2\pi m_T) \cdot d^2N/dydm_T$], of π^+ , π^- , K^+ , K^- , p , and \bar{p} produced at mid- y or mid- η in central Au-Au collisions at high $\sqrt{s_{NN}}$. The closed and open symbols represent respectively the experimental data of positively and negatively charged particles measured by (a)–(e) the E866 [25] and E895 [26, 27], (f) the E802 [28, 29], (g)–(o) the STAR [30, 31, 32], and (p)–(q) the PHENIX [33, 34] Collaborations marked in the panels which appear mostly [(g)–(q)] in Fig. 1 continued parts, where in Figs. 1(a)–1(d) the data for π^\pm and K^+ are taken from the E866 Collaboration [25] and the data for p are taken from the E895 Collaboration [26, 27]. The solid and dashed curves are our results fitted by Eq. (6) or (7) for positively and negatively charged particles respectively. The dot-dashed curves are our results fitted by using the weighted average parameter $\langle T \rangle$. The dotted curves and asterisks in Figs. 1(a)–1(f) represent the MC results for K^+ with high (10^6 particles) and low (10^4 particles) statistics respectively.

dashed curves, the least squares method is used to determine the best parameter values. The experimental global uncertainties used in the calculation of χ^2 are taken to be the root sum square of statistical uncertain-

ties and point-by-point systematic uncertainties. The best parameters are determined due to the limitation of the minimum χ^2 . The global uncertainties of parameters are obtained using the method of statistical simu-

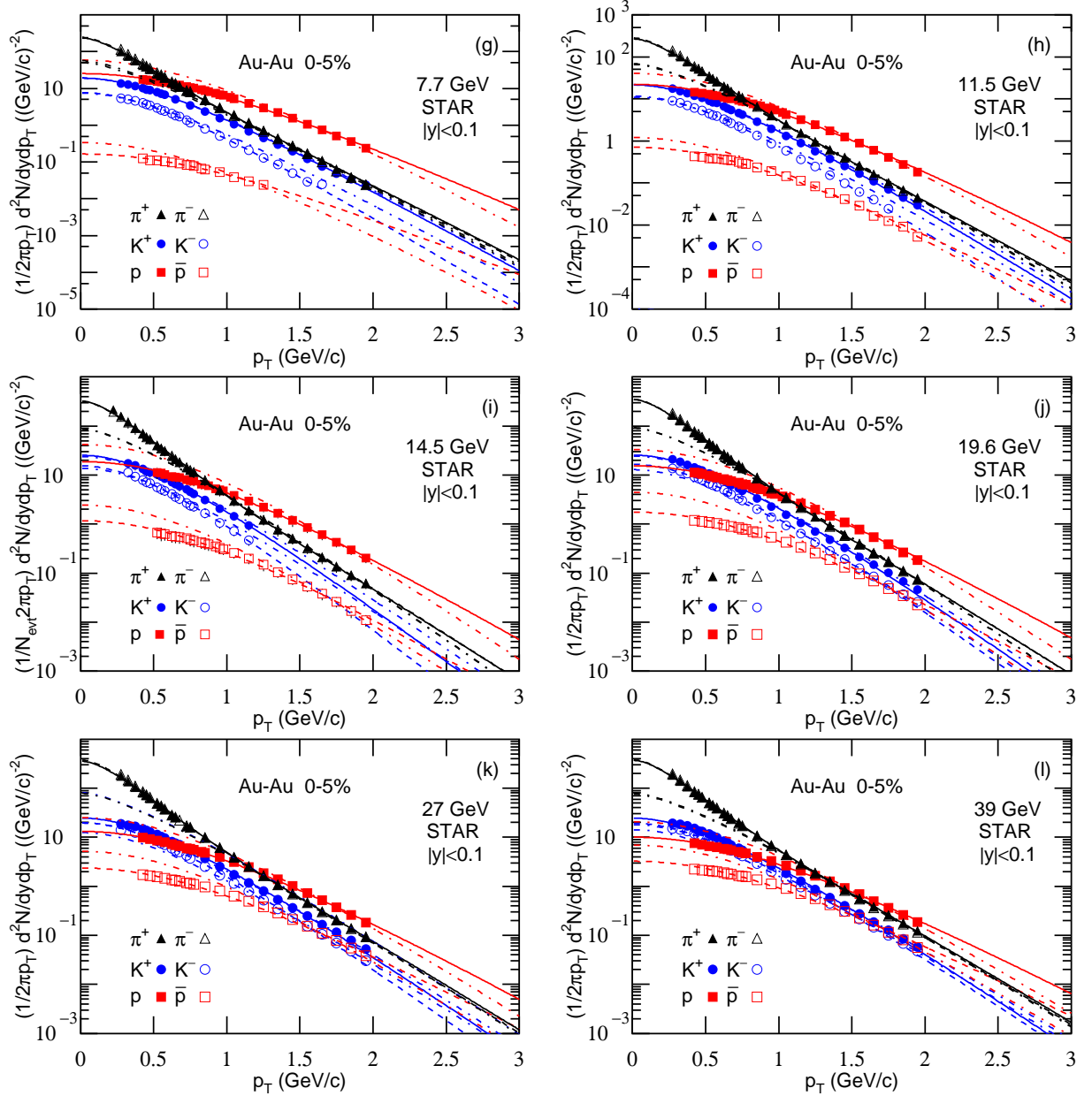


Fig. 1. Continued.

lation [62]. We note that χ^2 per dof (χ^2/dof) in a few cases is larger than 10, which renders that the fit is not too good. One can see that the (two-component) standard distribution fits approximately the p_T ($m_T - m_0$) spectra of π^\pm , K^\pm , p , and \bar{p} measured at mid- y or mid- η in central Au-Au collisions over an energy range from 2.7 to 200 GeV in most cases.

Figure 2 is similar to Fig. 1, but it showing the spectra of various particles produced at mid- y in central Pb-Pb collisions at high $\sqrt{s_{NN}}$, where the factor $(1/2\pi)$ on the vertical axis is removed in some cases and N_{evt} if

available denotes the particle number which can be removed. The symbols represent the experimental data measured by the NA49 [35, 36, 37] and ALICE [38] Collaborations. The values of various parameters, χ^2 , and dof for fitting the solid and dashed curves are listed in Table 2. Figure 3 is similar to Figs. 1 and 2, but it showing the spectra of various particles produced at mid- y or mid- η in INEL pp collisions at high center-of-mass energies \sqrt{s} , where the factor $(1/2\pi p_T)$ on the vertical axis is removed and the invariant cross-section $Ed^3\sigma/dp^3$ is used in some cases. The symbols represent the exper-

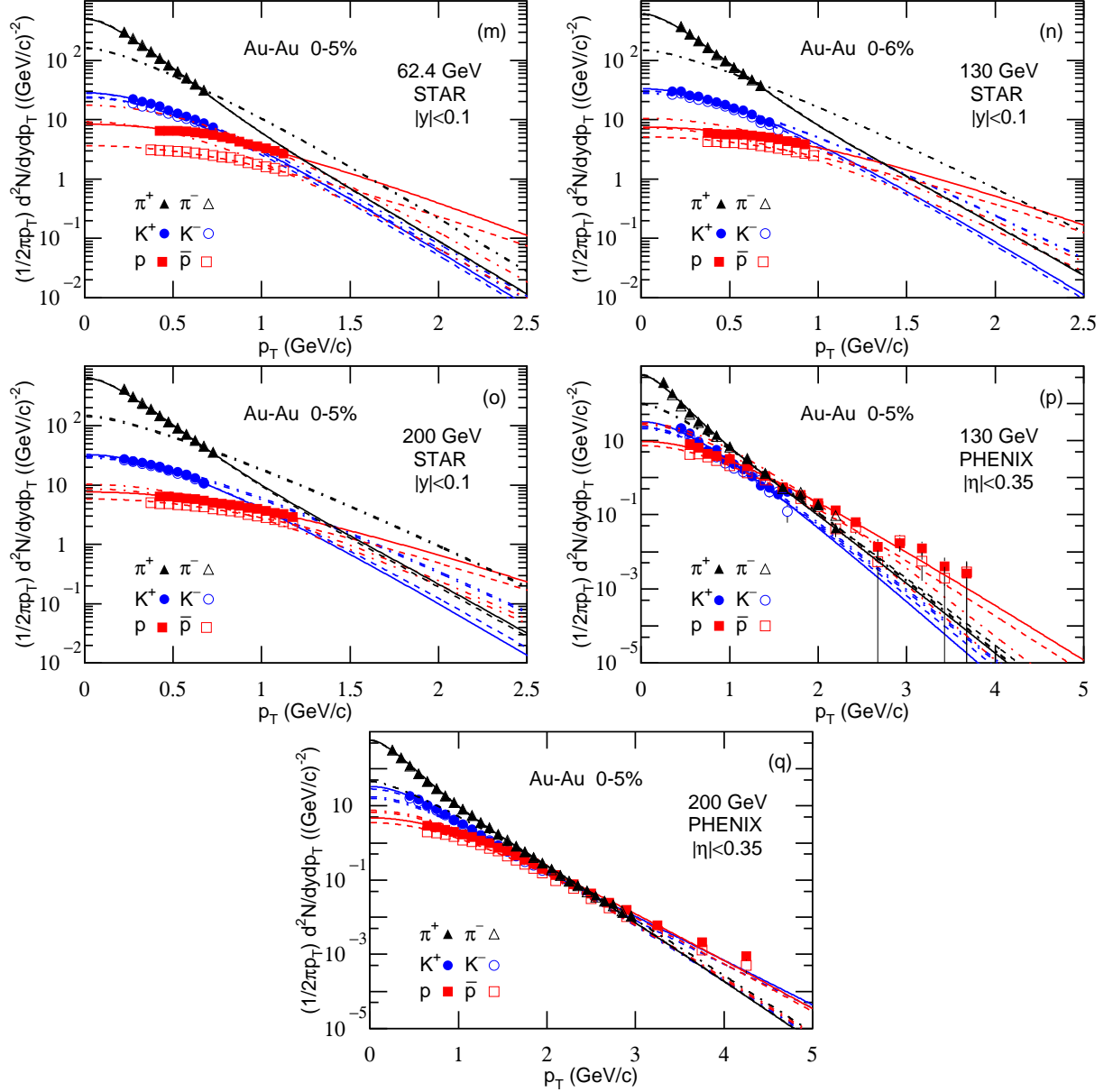


Fig. 1. Continued.

imental data measured by the NA61/SHINE [39, 40], PHENIX [41], and CMS [42, 43] Collaborations. The values of various parameters, χ^2 , and dof for fitting the solid and dashed curves are listed in Table 3, where the cross-section σ_0 is used as the normalization constant if the spectrum is $Ed^3\sigma/dp^3$. One can see that the (two-component) standard distribution fits approximately the p_T ($m_T - m_0$) spectra of π^\pm , K^\pm , p , and \bar{p} measured at mid- y or mid- η in central Pb-Pb and INEL pp collisions over an energy range from 6.3 to 13000 GeV in most cases.

To study the dependence of main parameter T on

collision energy $\sqrt{s_{NN}}$ or \sqrt{s} , the excitation functions of T for central Au-Au (Pb-Pb) collisions and INEL pp collisions are shown in Figs. 4(a) and 4(b) respectively. The results obtained from the spectra of π^+ , π^- , K^+ , K^- , p , and \bar{p} are displayed by different symbols marked in the panels. The asterisks represent $\langle T \rangle$ which is the average T by weighting different masses and yields of the six particles. In the case of one of the six particles is absent, $\langle T \rangle$ is not available. One can see that T and $\langle T \rangle$ increase with the increase of $\ln(\sqrt{s_{NN}})$ [$\ln(\sqrt{s})$]. Meanwhile, T increases with the increase of particle mass.

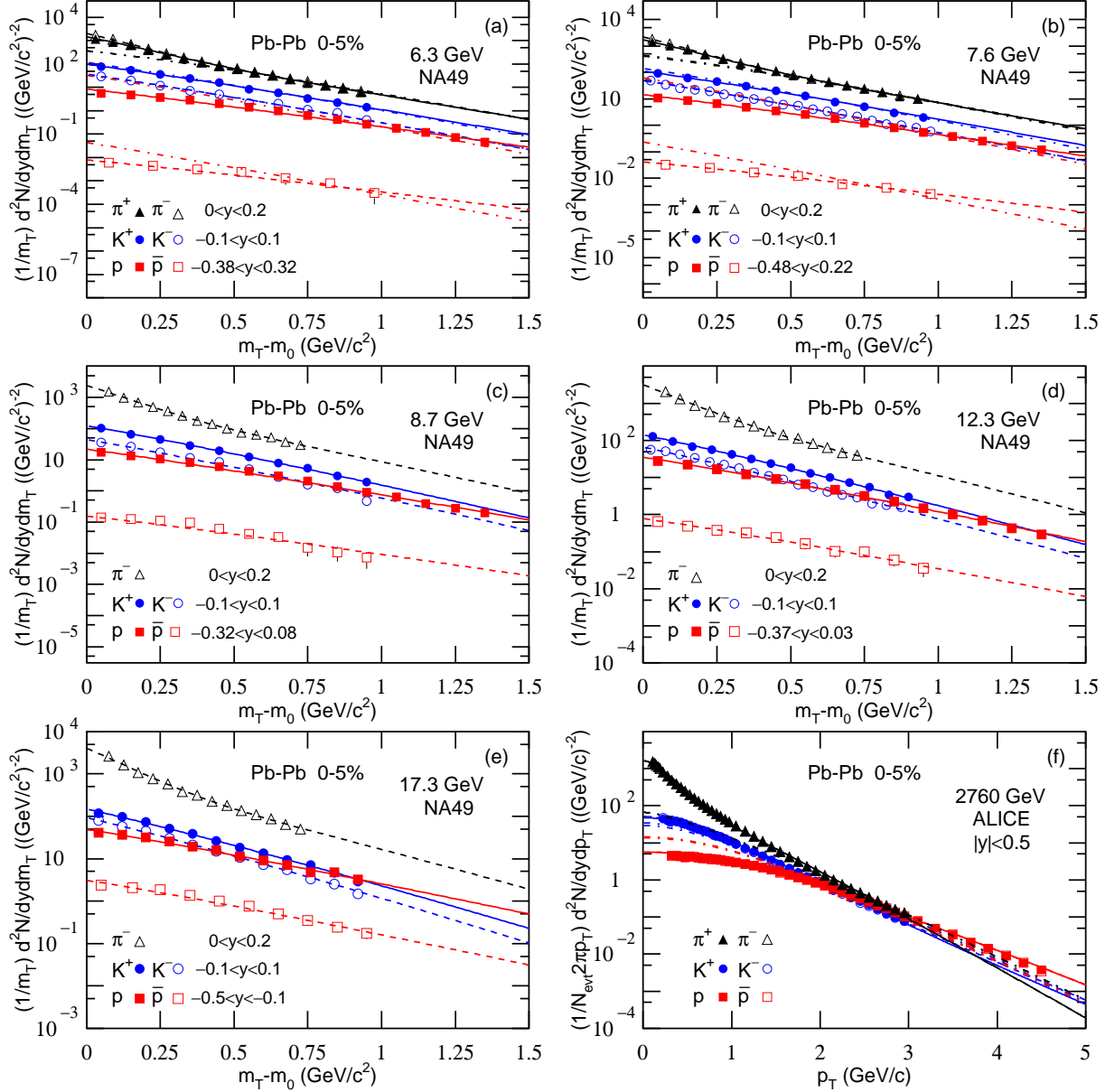


Fig. 2. Same as Fig. 1, but showing the spectra of various particles produced at mid- y in central Pb-Pb collisions at high $\sqrt{s_{NN}}$, where the factor $(1/2\pi)$ on the vertical axis is removed in some cases and N_{evt} if available denotes the particle number which can be removed. The symbols represent the experimental data measured by (a)–(e) the NA49 [35, 36, 37] and (f) the ALICE [38] Collaborations.

To better determine the kinetic freeze-out information, we now fit simultaneously the spectra of π^+ , π^- , K^+ , K^- , p , and \bar{p} in different p_T ranges using the same set of parameters. In Figs. 1–3, the dot-dashed curves are the results using the weighted average $\langle T \rangle$ which is energy dependent, though in fact we may use other T to obtain a little better result in some cases. In the refit, the normalization constant N_0 for different spectra is adjustable to fit suitable p_T range. In spite of

mass dependent (two-)temperature in non-simultaneous fit, the simultaneous fit is done using the same and only set of $\langle T \rangle$ for the six species of particles at each energy. That is to say that we use one component function to fit the spectra of the six species of particles at each energy. And the temperature is the same for each particle and the normalization factor is adjusted. It seems that our treatment is not a fair comparison of the non-simultaneous fit and simultaneous fit, where the non-

Table 1. Values of free parameters (T_1 , T_2 if available, k), derived parameter [$T = kT_1 + (1 - k)T_2$], normalization constant (N_0), χ^2 and dof corresponding to the solid and dashed curves in Fig. 1 in which different data in central Au-Au collisions are measured in different mid-(pseudo)rapidity intervals at different energies by different collaborations. The values for positive and negative particles are listed in terms of value₁/value₂, if the two values appear together.

Collab.	$\sqrt{s_{NN}}$ (GeV)	Particle	T_1 (MeV)	T_2 (MeV)	k	T (MeV)	N_0	χ^2	dof
E866/E895	2.7	π^\pm	$80 \pm 4/62 \pm 4$	$190 \pm 5/165 \pm 5$	$0.88 \pm 0.02/0.88 \pm 0.02$	$93 \pm 4/74 \pm 4$	$1.19 \pm 0.03/2.08 \pm 0.04$	15/22	19/26
		K^+	128 ± 4	—	1	128 ± 4	0.16 ± 0.01	4	8
		p	192 ± 6	—	1	192 ± 3	1.22 ± 0.02	278	38
	3.32	π^\pm	$85 \pm 4/71 \pm 4$	$209 \pm 12/163 \pm 8$	$0.78 \pm 0.03/0.79 \pm 0.02$	$112 \pm 4/90 \pm 4$	$2.84 \pm 0.02/3.96 \pm 0.04$	8/32	24/36
		K^+	131 ± 5	—	1	131 ± 5	1.35 ± 0.02	2	10
		p	213 ± 4	—	1	213 ± 4	6.99 ± 0.05	401	38
	3.84	π^\pm	$88 \pm 3/75 \pm 3$	$230 \pm 5/170 \pm 5$	$0.74 \pm 0.03/0.73 \pm 0.02$	$125 \pm 3/101 \pm 3$	$4.00 \pm 0.03/5.16 \pm 0.04$	6/54	19/36
		K^+	167 ± 5	—	1	167 ± 5	3.08 ± 0.01	1	9
		p	210 ± 4	—	1	210 ± 4	6.32 ± 0.05	592	38
	4.3	π^\pm	$90 \pm 4/77 \pm 4$	$229 \pm 4/171 \pm 3$	$0.70 \pm 0.02/0.71 \pm 0.01$	$132 \pm 3/104 \pm 3$	$4.88 \pm 0.03/6.30 \pm 0.04$	10/50	16/36
		K^+	172 ± 5	—	1	172 ± 5	5.59 ± 0.06	1	7
		p	224 ± 5	—	1	224 ± 5	6.09 ± 0.07	204	38
	4.85	π^+	96 ± 3	214 ± 5	0.73 ± 0.03	128 ± 3	319.96 ± 1.12	1	16
		K^+	170 ± 5	—	1	170 ± 5	4.66 ± 0.10	2	9
E802	5.03	π^\pm	$103 \pm 3/93 \pm 4$	$210 \pm 4/194 \pm 5$	$0.73 \pm 0.03/0.72 \pm 0.02$	$132 \pm 2/121 \pm 3$	$22.00 \pm 3.00/27.12 \pm 3.00$	17/45	30/29
		K^\pm	$172 \pm 5/166 \pm 5$	—/—	1/1	$172 \pm 5/166 \pm 5$	$2.28 \pm 0.05/0.45 \pm 0.01$	3/4	9/9
		p	230 ± 4	—	1	230 ± 4	12.59 ± 1.03	136	27
STAR	7.7	π^\pm	$115 \pm 10/115 \pm 10$	$199 \pm 3/198 \pm 3$	$0.68 \pm 0.02/0.70 \pm 0.02$	$142 \pm 10/140 \pm 9$	$18.21 \pm 3.00/18.83 \pm 4.00$	14/16	22/22
		K^\pm	$185 \pm 5/170 \pm 5$	—/—	1/1	$185 \pm 5/170 \pm 5$	$4.19 \pm 0.50/1.49 \pm 0.30$	11/12	21/21
		p/\bar{p}	$226 \pm 7/251 \pm 6$	—/—	1/1	$226 \pm 7/251 \pm 6$	$11.01 \pm 0.70/0.084 \pm 0.002$	11/3	27/13
	11.5	π^\pm	$124 \pm 10/123 \pm 10$	$211 \pm 3/209 \pm 3$	$0.72 \pm 0.02/0.73 \pm 0.02$	$148 \pm 9/146 \pm 9$	$22.82 \pm 0.50/23.58 \pm 0.70$	8/10	22/22
		K^\pm	$190 \pm 5/178 \pm 5$	—/—	1/1	$190 \pm 5/178 \pm 5$	$4.93 \pm 0.20/2.43 \pm 0.10$	7/4	23/21
		p/\bar{p}	$223 \pm 7/223 \pm 7$	—/—	1/1	$223 \pm 7/223 \pm 7$	$9.41 \pm 0.60/0.30 \pm 0.01$	13/32	26/21
	14.5	π^\pm	$124 \pm 10/123 \pm 10$	$213 \pm 3/212 \pm 3$	$0.72 \pm 0.02/0.70 \pm 0.02$	$149 \pm 9/150 \pm 9$	$27.58 \pm 1.30/27.38 \pm 1.20$	1/1	24/24
		K^\pm	$183 \pm 9/173 \pm 8$	—/—	1/1	$183 \pm 9/173 \pm 8$	$5.49 \pm 0.03/3.07 \pm 0.02$	1/1	16/16
		p/\bar{p}	$230 \pm 9/229 \pm 7$	—/—	1/1	$230 \pm 9/229 \pm 7$	$8.39 \pm 0.06/0.52 \pm 0.01$	1/1	23/23
	19.6	π^\pm	$124 \pm 10/123 \pm 10$	$216 \pm 3/216 \pm 3$	$0.70 \pm 0.03/0.70 \pm 0.02$	$152 \pm 9/151 \pm 9$	$29.98 \pm 5.10/30.00 \pm 5.40$	6/8	22/21
		K^\pm	$193 \pm 6/189 \pm 5$	—/—	1/1	$193 \pm 6/189 \pm 5$	$5.99 \pm 0.05/3.77 \pm 0.02$	35/36	24/24
		p/\bar{p}	$237 \pm 8/243 \pm 9$	—/—	1/1	$237 \pm 8/243 \pm 9$	$7.17 \pm 0.07/0.85 \pm 0.01$	6/15	27/20
	27	π^\pm	$125 \pm 10/124 \pm 10$	$220 \pm 3/217 \pm 3$	$0.68 \pm 0.02/0.69 \pm 0.02$	$155 \pm 10/153 \pm 9$	$31.86 \pm 4.10/32.86 \pm 4.50$	5/10	21/22
		K^\pm	$199 \pm 6/190 \pm 6$	—/—	1/1	$199 \pm 6/190 \pm 6$	$6.07 \pm 0.05/4.57 \pm 0.03$	19/32	24/22
		p/\bar{p}	$242 \pm 10/251 \pm 12$	—/—	1/1	$242 \pm 10/251 \pm 12$	$6.31 \pm 0.07/1.20 \pm 0.01$	6/15	21/20
	39	π^\pm	$125 \pm 10/125 \pm 10$	$225 \pm 3/224 \pm 3$	$0.66 \pm 0.02/0.68 \pm 0.01$	$159 \pm 9/157 \pm 9$	$33.80 \pm 5.10/34.12 \pm 5.30$	5/6	22/22
		K^\pm	$203 \pm 7/203 \pm 6$	—/—	1/1	$203 \pm 7/203 \pm 6$	$6.23 \pm 0.07/4.91 \pm 0.03$	16/28	24/24
		p/\bar{p}	$257 \pm 11/259 \pm 10$	—/—	1/1	$257 \pm 11/259 \pm 10$	$4.91 \pm 0.05/1.72 \pm 0.01$	5/19	20/21
	62.4	π^\pm	$123 \pm 10/123 \pm 10$	$220 \pm 3/220 \pm 3$	$0.71 \pm 0.01/0.72 \pm 0.01$	$151 \pm 9/150 \pm 9$	$42.30 \pm 5.12/43.12 \pm 5.20$	22/25	6/6
		K^\pm	$210 \pm 8/210 \pm 8$	—/—	1/1	$210 \pm 8/210 \pm 8$	$7.61 \pm 0.30/6.50 \pm 0.27$	1/10	8/8
		p/\bar{p}	$320 \pm 11/346 \pm 11$	—/—	1/1	$320 \pm 11/346 \pm 11$	$6.25 \pm 0.20/3.10 \pm 0.05$	170/102	13/14
	130	π^\pm	$120 \pm 6/123 \pm 5$	$232 \pm 9/234 \pm 10$	$0.68 \pm 0.01/0.69 \pm 0.01$	$156 \pm 6/157 \pm 5$	$51.86 \pm 5.22/51.92 \pm 5.66$	39/74	6/6
		K^\pm	$216 \pm 8/214 \pm 9$	—/—	1/1	$216 \pm 8/214 \pm 9$	$9.32 \pm 0.28/8.48 \pm 0.15$	2/3	10/11
		p/\bar{p}	$353 \pm 9/359 \pm 8$	—/—	1/1	$353 \pm 9/359 \pm 8$	$6.64 \pm 0.15/4.68 \pm 0.11$	57/134	10/11
	200	π^\pm	$126 \pm 9/127 \pm 10$	$236 \pm 12/235 \pm 12$	$0.67 \pm 0.01/0.70 \pm 0.01$	$162 \pm 9/159 \pm 10$	$59.00 \pm 3.33/59.12 \pm 3.70$	18/23	7/7
		K^\pm	$221 \pm 13/230 \pm 13$	—/—	1/1	$221 \pm 13/230 \pm 13$	$9.48 \pm 0.23/9.50 \pm 0.25$	3/2	8/8
		p/\bar{p}	$376 \pm 16/372 \pm 11$	—/—	1/1	$376 \pm 16/372 \pm 11$	$7.56 \pm 0.18/5.68 \pm 0.14$	4/31	14/15
PHENIX	130	π^\pm	$123 \pm 10/121 \pm 10$	$220 \pm 3/229 \pm 3$	$0.70 \pm 0.02/0.73 \pm 0.01$	$152 \pm 9/150 \pm 10$	$167.72 \pm 10.50/167.72 \pm 11.00$	146/182	10/10
		K^\pm	$201 \pm 10/213 \pm 13$	—/—	1/1	$210 \pm 10/213 \pm 13$	$27.31 \pm 2.10/21.36 \pm 1.53$	17/15	11/11
		p/\bar{p}	$276 \pm 10/267 \pm 11$	—/—	1/1	$276 \pm 10/267 \pm 11$	$18.77 \pm 1.25/13.80 \pm 1.16$	15/13	15/15
	200	π^\pm	$136 \pm 4/136 \pm 4$	$259 \pm 3/259 \pm 3$	$0.74 \pm 0.02/0.73 \pm 0.02$	$168 \pm 4/169 \pm 4$	$199.02 \pm 16.01/196.43 \pm 15.10$	286/205	24/24
		K^\pm	$197 \pm 12/215 \pm 13$	$339 \pm 11/346 \pm 12$	$0.73 \pm 0.01/0.81 \pm 0.01$	$235 \pm 12/240 \pm 13$	$32.56 \pm 2.10/30.04 \pm 2.00$	28/22	12/12
		p/\bar{p}	$311 \pm 7/314 \pm 8$	—/—	1/1	$311 \pm 7/314 \pm 8$	$11.49 \pm 0.72/8.62 \pm 0.06$	69/90	20/20

Table 2. The same as Table 1, but showing the results for central Pb-Pb collisions which are shown in Fig. 2.

Collab.	$\sqrt{s_{NN}}$ (GeV)	Particle	T_1 (MeV)	T_2 (MeV)	k	T (MeV)	N_0	χ^2	dof
NA49	6.3	π^\pm	$97 \pm 5/86 \pm 4$	$185 \pm 5/181 \pm 4$	$0.64 \pm 0.02/0.65 \pm 0.01$	$129 \pm 5/119 \pm 4$	$14.50 \pm 1.10/16.98 \pm 1.23$	69/43	12/12
		K^\pm	$182 \pm 5/172 \pm 8$	—/—	1/1	$182 \pm 5/172 \pm 8$	$3.33 \pm 0.03/1.14 \pm 0.01$	22/25	8/8
		p/\bar{p}	$227 \pm 10/259 \pm 12$	—/—	1/1	$227 \pm 10/259 \pm 12$	$2.05 \pm 0.01/0.0023 \pm 0.0001$	14/2	12/5
	7.6	π^\pm	$97 \pm 6/86 \pm 4$	$195 \pm 4/187 \pm 3$	$0.61 \pm 0.01/0.58 \pm 0.01$	$135 \pm 6/128 \pm 4$	$17.44 \pm 1.15/19.50 \pm 2.20$	24/26	12/12
		K^\pm	$193 \pm 5/181 \pm 6$	—/—	1/1	$193 \pm 5/181 \pm 6$	$4.11 \pm 0.33/1.63 \pm 0.05$	30/60	8/18
		p/\bar{p}	$242 \pm 6/284 \pm 11$	—/—	1/1	$242 \pm 6/284 \pm 11$	$3.74 \pm 0.08/0.014 \pm 0.001$	10/1	12/5
	8.7	π^-	84 ± 5	188 ± 4	0.56 ± 0.02	130 ± 5	21.40 ± 0.71	44	10
		K^\pm	$185 \pm 6/187 \pm 5$	—/—	1/1	$185 \pm 6/187 \pm 5$	$4.30 \pm 0.05/1.58 \pm 0.01$	37/33	8/8
		p/\bar{p}	$244 \pm 7/280 \pm 10$	—/—	1/1	$244 \pm 7/280 \pm 10$	$3.56 \pm 0.03/0.030 \pm 0.001$	14/10	12/8
	12.3	π^-	84 ± 6	189 ± 5	0.56 ± 0.01	130 ± 6	27.80 ± 2.11	60	10
		K^\pm	$185 \pm 7/183 \pm 5$	—/—	1/1	$185 \pm 7/183 \pm 5$	$4.92 \pm 0.08/2.24 \pm 0.02$	10/54	12/16
		p/\bar{p}	$244 \pm 8/260 \pm 14$	—/—	1/1	$244 \pm 8/260 \pm 14$	$5.48 \pm 0.09/0.13 \pm 0.01$	5/1	12/8
	17.3	π^-	84 ± 6	200 ± 5	0.57 ± 0.01	134 ± 6	35.80 ± 1.80	47	10
		K^\pm	$193 \pm 7/185 \pm 6$	—/—	1/1	$193 \pm 7/185 \pm 6$	$5.52 \pm 0.30/3.26 \pm 0.09$	27/17	10/10
		p/\bar{p}	$280 \pm 13/280 \pm 14$	—/—	1/1	$280 \pm 13/280 \pm 14$	$8.86 \pm 0.23/0.56 \pm 0.03$	9/3	10/8
ALICE	2760	π^\pm	$127 \pm 4/127 \pm 4$	$309 \pm 3/309 \pm 3$	$0.65 \pm 0.01/0.65 \pm 0.01$	$191 \pm 4/191 \pm 4$	$762.61 \pm 33.11/762.61 \pm 33.11$	74/73	37/37
		K^\pm	$290 \pm 6/275 \pm 4$	$409 \pm 10/409 \pm 3$	$0.82 \pm 0.02/0.75 \pm 0.02$	$311 \pm 6/309 \pm 4$	$108.82 \pm 5.3/108.49 \pm 5.1$	49/4	32/32
		p/\bar{p}	$428 \pm 9/428 \pm 6$	—/—	1/1	$428 \pm 9/428 \pm 6$	$32.81 \pm 2.10/32.91 \pm 1.91$	63/49	40/40

Table 3. The same as Table 1, but showing the results for INEL pp collisions which are shown in Fig. 3, where the normalization constant is σ_0 for the cases of 62.4 and 200 GeV presented in Figs. 3(f) and 3(g) respectively.

Collab.	\sqrt{s} (GeV)	Particle	T_1 (MeV)	T_2 (MeV)	k	T (MeV)	N_0 (σ_0)	χ^2	dof
NA61/SHINE	6.3	π^-	110 ± 7	169 ± 9	0.82 ± 0.01	121 ± 7	0.086 ± 0.006	12	14
		K^\pm	$113 \pm 6/123 \pm 6$	—/—	1/1	$113 \pm 6/123 \pm 6$	$0.0096 \pm 0.0003/0.0030 \pm 0.0001$	2/1	4/8
		p	125 ± 5	—	1	125 ± 5	0.027 ± 0.001	69	5
	7.7	π^\pm	$103 \pm 10/113 \pm 10$	$177 \pm 9/178 \pm 9$	$0.78 \pm 0.01/0.81 \pm 0.01$	$119 \pm 10/125 \pm 10$	$0.16 \pm 0.01/0.098 \pm 0.003$	1/16	1/16
		K^\pm	$131 \pm 6/127 \pm 6$	—/—	1/1	$131 \pm 6/127 \pm 6$	$0.0013 \pm 0.0001/0.0050 \pm 0.0002$	4/1	7/5
		p/\bar{p}	$136 \pm 10/104 \pm 12$	—/—	1/1	$136 \pm 10/104 \pm 12$	$0.027 \pm 0.002/0.00066 \pm 0.00001$	4/5	9/7
	8.8	π^\pm	$105 \pm 10/113 \pm 10$	$182 \pm 9/178 \pm 9$	$0.78 \pm 0.02/0.81 \pm 0.02$	$122 \pm 10/125 \pm 10$	$0.16 \pm 0.01/0.11 \pm 0.01$	1/33	2/18
		K^\pm	$126 \pm 6/123 \pm 6$	—/—	1/1	$126 \pm 6/123 \pm 6$	$0.013 \pm 0.001/0.0056 \pm 0.0002$	24/6	9/7
		p/\bar{p}	$136 \pm 9/102 \pm 12$	—/—	1/1	$136 \pm 9/102 \pm 12$	$0.027 \pm 0.001/0.00078 \pm 0.00004$	1/3	9/3
	12.3	π^\pm	$108 \pm 10/113 \pm 10$	$190 \pm 9/184 \pm 9$	$0.77 \pm 0.02/0.79 \pm 0.01$	$127 \pm 10/128 \pm 10$	$0.16 \pm 0.01/0.12 \pm 0.01$	1/23	2/16
		K^\pm	$135 \pm 6/127 \pm 6$	—/—	1/1	$135 \pm 6/127 \pm 6$	$0.015 \pm 0.001/0.0074 \pm 0.0003$	10/9	8/7
		p/\bar{p}	$150 \pm 10/106 \pm 12$	—/—	1/1	$150 \pm 10/106 \pm 12$	$0.017 \pm 0.001/0.0018 \pm 0.0001$	6/9	11/9
	17.3	π^\pm	$111 \pm 8/113 \pm 10$	$180 \pm 9/190 \pm 8$	$0.76 \pm 0.01/0.79 \pm 0.01$	$128 \pm 8/129 \pm 10$	$0.16 \pm 0.01/0.13 \pm 0.01$	1/8	1/19
		K^\pm	$130 \pm 6/138 \pm 6$	—/—	1/1	$130 \pm 6/138 \pm 6$	$0.015 \pm 0.001/0.010 \pm 0.001$	2/2	8/8
		p/\bar{p}	$150 \pm 10/128 \pm 12$	—/—	1/1	$50 \pm 10/128 \pm 12$	$0.015 \pm 0.001/0.0034 \pm 0.0001$	2/4	8/8
PHENIX	62.4	π^\pm	$118 \pm 5/113 \pm 4$	$240 \pm 4/229 \pm 4$	$0.82 \pm 0.01/0.81 \pm 0.01$	$140 \pm 5/135 \pm 4$	$17.21 \pm 3.00/18.40 \pm 5.00$	14/25	22/22
		K^\pm	$147 \pm 6/149 \pm 5$	$284 \pm 6/278 \pm 5$	$0.76 \pm 0.01/0.78 \pm 0.01$	$180 \pm 6/177 \pm 5$	$1.84 \pm 0.50/1.58 \pm 0.40$	5/2	12/12
		p/\bar{p}	$161 \pm 10/163 \pm 12$	$283 \pm 4/278 \pm 5$	$0.80 \pm 0.00/0.81 \pm 0.01$	$182 \pm 10/185 \pm 11$	$1.05 \pm 0.40/0.57 \pm 0.03$	12/14	23/23
	200	π^\pm	$117 \pm 5/115 \pm 5$	$278 \pm 5/273 \pm 5$	$0.85 \pm 0.00/0.82 \pm 0.01$	$141 \pm 5/145 \pm 5$	$25.26 \pm 5.00/22.61 \pm 3.00$	101/83	23/23
		K^\pm	$151 \pm 4/149 \pm 5$	$303 \pm 8/301 \pm 5$	$0.72 \pm 0.01/0.72 \pm 0.01$	$193 \pm 4/192 \pm 5$	$2.78 \pm 0.40/2.76 \pm 0.70$	10/7	12/12
		p/\bar{p}	$162 \pm 5/160 \pm 6$	$316 \pm 7/312 \pm 5$	$0.73 \pm 0.00/0.76 \pm 0.00$	$204 \pm 5/197 \pm 6$	$1.23 \pm 0.20/1.09 \pm 0.10$	108/91	30/30
CMS	900	π^\pm	$115 \pm 4/117 \pm 5$	$264 \pm 5/270 \pm 6$	$0.68 \pm 0.01/0.68 \pm 0.01$	$163 \pm 4/165 \pm 5$	$3.76 \pm 0.50/3.70 \pm 0.50$	13/12	18/18
		K^\pm	$156 \pm 6/154 \pm 6$	$343 \pm 10/340 \pm 10$	$0.59 \pm 0.01/0.58 \pm 0.01$	$233 \pm 6/232 \pm 6$	$0.47 \pm 0.03/0.46 \pm 0.03$	4/6	13/13
		p/\bar{p}	$177 \pm 6/177 \pm 5$	$331 \pm 9/328 \pm 8$	$0.55 \pm 0.01/0.56 \pm 0.01$	$246 \pm 6/243 \pm 5$	$0.21 \pm 0.02/0.20 \pm 0.01$	19/17	23/23
	2760	π^\pm	$116 \pm 3/116 \pm 4$	$275 \pm 5/281 \pm 5$	$0.64 \pm 0.01/0.65 \pm 0.01$	$173 \pm 3/174 \pm 4$	$4.68 \pm 0.90/4.60 \pm 0.80$	19/14	18/18
		K^\pm	$165 \pm 7/164 \pm 8$	$351 \pm 9/350 \pm 9$	$0.56 \pm 0.01/0.56 \pm 0.01$	$247 \pm 7/246 \pm 8$	$0.60 \pm 0.03/0.59 \pm 0.03$	5/10	13/13
		p/\bar{p}	$182 \pm 6/183 \pm 7$	$406 \pm 8/392 \pm 7$	$0.54 \pm 0.01/0.55 \pm 0.01$	$285 \pm 6/277 \pm 7$	$0.27 \pm 0.01/0.26 \pm 0.01$	28/32	23/23
	7000	π^\pm	$116 \pm 4/115 \pm 4$	$292 \pm 5/288 \pm 4$	$0.63 \pm 0.02/0.62 \pm 0.01$	$181 \pm 4/181 \pm 4$	$5.82 \pm 0.80/5.76 \pm 0.80$	34/22	18/18
		K^\pm	$178 \pm 6/175 \pm 6$	$420 \pm 10/393 \pm 10$	$0.59 \pm 0.02/0.56 \pm 0.02$	$277 \pm 6/271 \pm 6$	$0.76 \pm 0.03/0.75 \pm 0.03$	3/8	13/13
		p/\bar{p}	$217 \pm 7/202 \pm 7$	$429 \pm 9/430 \pm 9$	$0.57 \pm 0.02/0.53 \pm 0.01$	$308 \pm 7/309 \pm 7$	$0.34 \pm 0.02/0.33 \pm 0.02$	28/22	23/23
	13000	π^\pm	$114 \pm 4/114 \pm 6$	$300 \pm 5/291 \pm 6$	$0.61 \pm 0.01/0.60 \pm 0.01$	$187 \pm 4/185 \pm 6$	$5.46 \pm 0.70/5.38 \pm 0.60$	9/10	18/18
		K^\pm	$180 \pm 10/180 \pm 10$	$360 \pm 12/383 \pm 12$	$0.59 \pm 0.01/0.60 \pm 0.01$	$254 \pm 10/261 \pm 10$	$0.65 \pm 0.03/0.65 \pm 0.03$	3/2	13/13
		p/\bar{p}	$229 \pm 10/231 \pm 11$	$425 \pm 3/425 \pm 9$	$0.63 \pm 0.01/0.62 \pm 0.01$	$302 \pm 10/305 \pm 10$	$0.30 \pm 0.02/0.29 \pm 0.02$	25/19	22/22

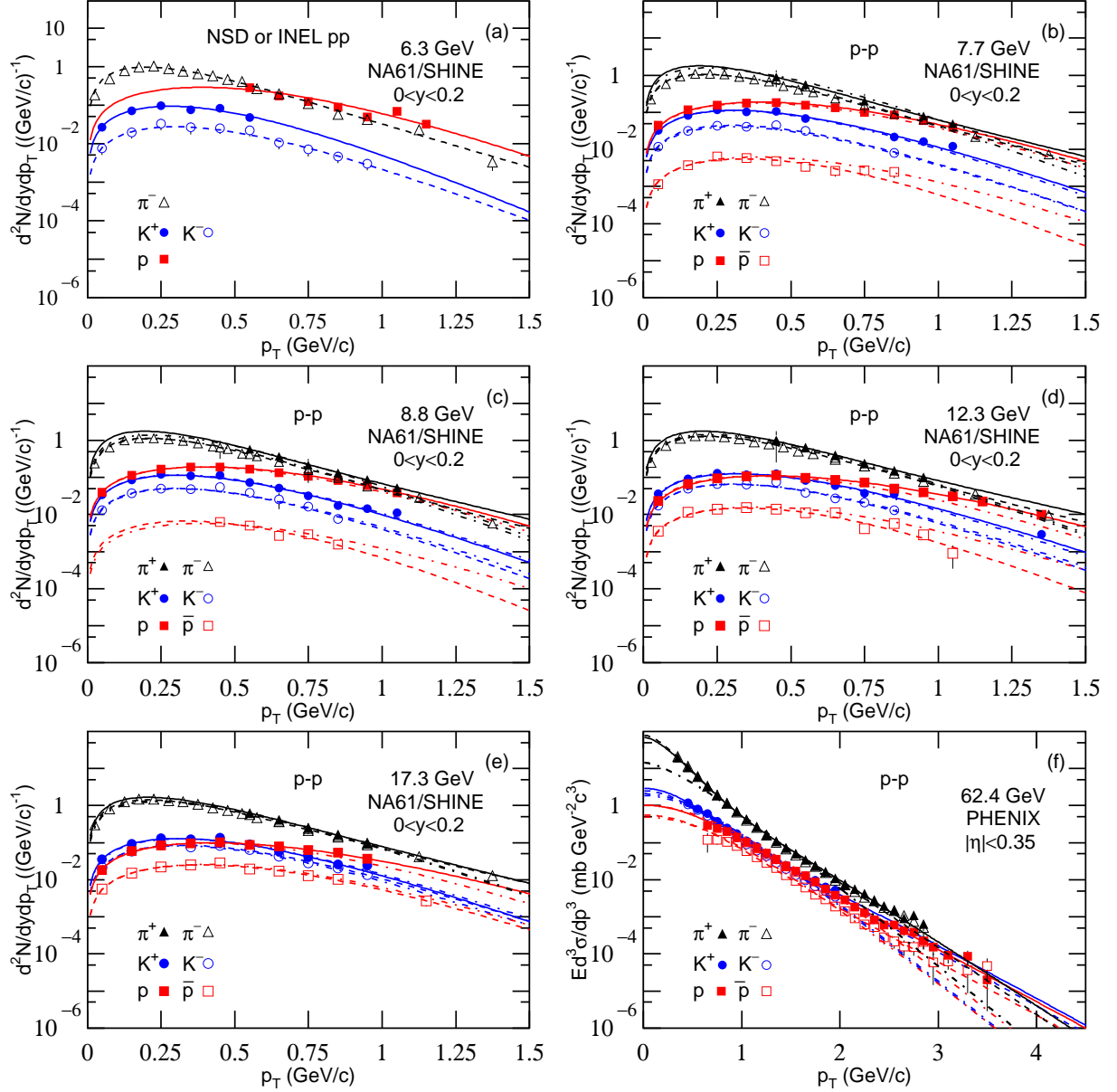


Fig. 3. Same as Fig. 1, but showing the spectra of various particles produced at mid- y or mid- η in INEL pp collisions at high center-of-mass energies \sqrt{s} , where the factor $(1/2\pi p_T)$ on the vertical axis is removed and the invariant cross-section $Ed^3\sigma/dp^3$ is used in some cases. The symbols represent the experimental data measured by (a)–(e) the NA61/SHINE [39, 40], (f)–(g) the PHENIX [41], and (h)–(k) the CMS [42, 43] Collaborations, where panels (g)–(k) appear in Fig. 3 continued part.

simultaneous fit uses the two-component in some cases. However, the simultaneous fit seeks for the same temperature which does not allow the two-component for some particles due to other particles corresponding to one component. In our opinion, our comparison is fair for the non-simultaneous fit and simultaneous fit. One can see that the same set of $\langle T \rangle$ can fit only a part of p_T range in some cases. The fit results using the same set

of parameters are not ideal. These results do not support the single scenario for kinetic freeze-out. We are not inclined to fit simultaneously the spectra of different particles. Conversely, we use different T for different spectra in this paper.

Figures 5(a) and 5(b) [5(c) and 5(d)] are similar to Figs. 4(a) and 4(b) respectively, but they showing the excitation functions of T_0 (β_T) and $\langle T_0 \rangle$ ($\langle \beta_T \rangle$). Figures

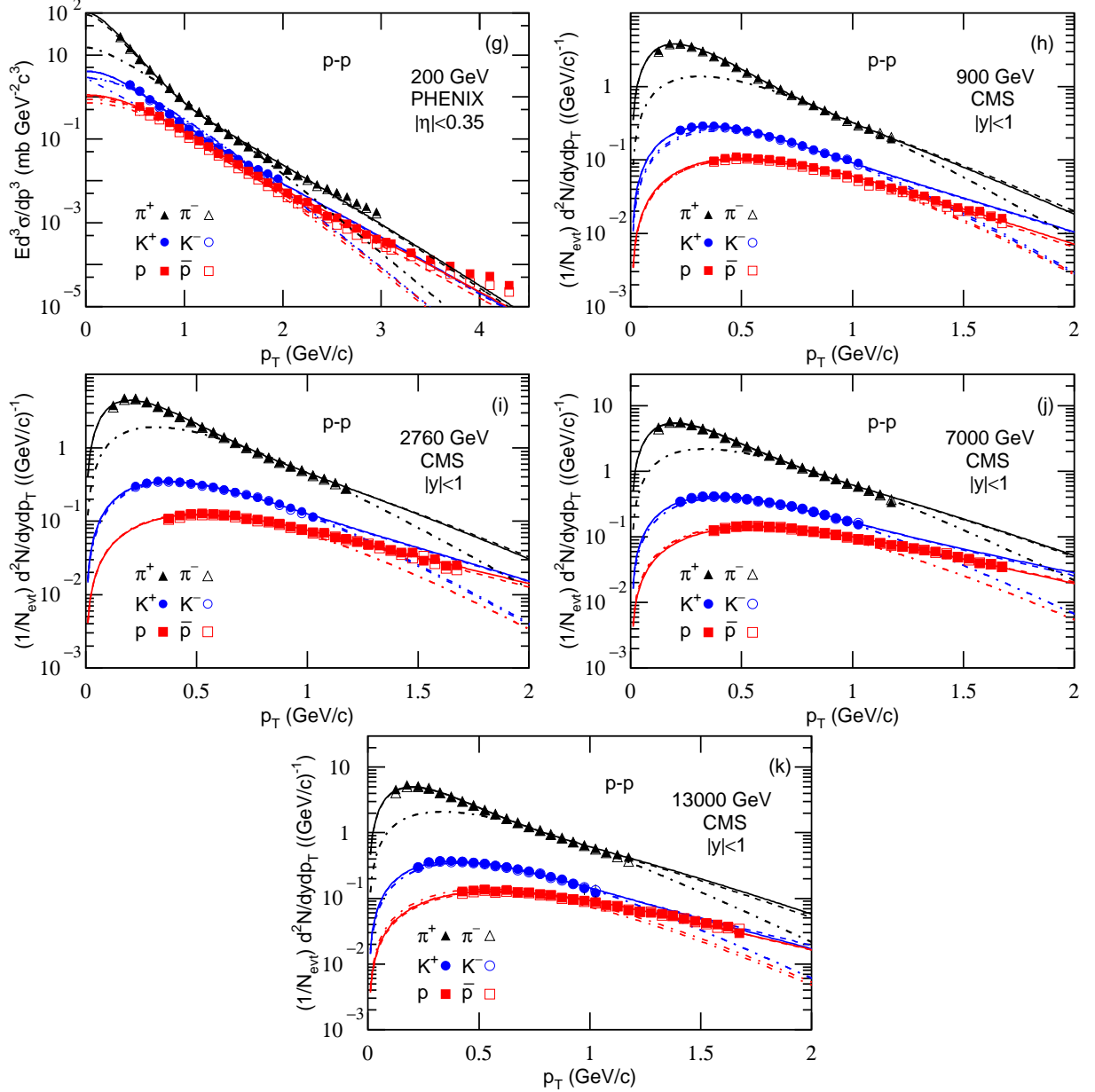


Fig. 3. Continued.

6(a) and 6(b) are also similar to Figs. 4(a) and 4(b) respectively, but they showing the excitation functions of T_i and $\langle T_i \rangle$. One can see that T_0 , $\langle T_0 \rangle$, β_T , $\langle \beta_T \rangle$, T_i , and $\langle T_i \rangle$ increase with the increase of $\ln(\sqrt{s_{NN}})$ [$\ln(\sqrt{s})$] in general, and T_0 for pion emission and $\langle T_0 \rangle$ appears the trend of saturation at the RHIC and LHC. Meanwhile, T_0 , $\langle T_0 \rangle$, T_i , and $\langle T_i \rangle$ increase, and β_T and $\langle \beta_T \rangle$ decrease, with the increase of particle mass.

It is regretful that some particles are absent in experimental measurements at the energies blow 10 GeV. This renders that $\langle T \rangle$, $\langle T_0 \rangle$, $\langle \beta_T \rangle$, and $\langle T_i \rangle$ are not avail-

able in the energy range of several GeV. From the trends of available T , T_0 , β_T , and T_i , we may estimate that $\langle T \rangle$, $\langle T_0 \rangle$, $\langle \beta_T \rangle$, and $\langle T_i \rangle$ increase (quickly) with the increase of $\ln(\sqrt{s_{NN}})$ [$\ln(\sqrt{s})$] in the energy range of several GeV. In particular, some excitation functions show little peak around 10 GeV, which should be studied further in future. Meanwhile, we hope to obtain more data in the energy range of several GeV in future.

It should be noted that since empirical Eq. (18) is essential for obtaining the energy dependence of T_0 and β_T , it seems that one can obtain arbitrary results by

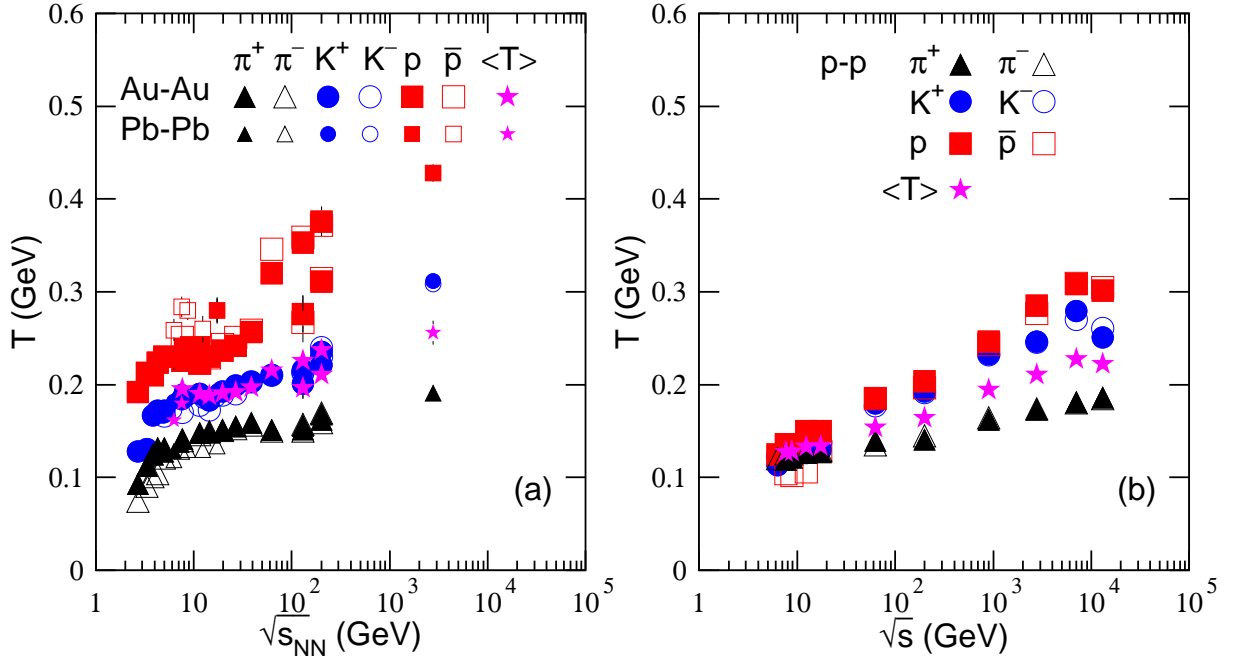


Fig. 4. Excitation functions of T and $\langle T \rangle$ in (a) central Au-Au (Pb-Pb) collisions and (b) INEL pp collisions. The symbols corresponding to identified particles are extracted from experimental spectra.

choosing another parametrization of k_0 . In particular, it seems possible to choose a parametrization of k_0 so that π^+ (π^-), K^+ (K^-), and p (\bar{p}) could have similar T_0 and β_T even though the combined temperature T (in Fig. 4) for these particles are quite different. This case corresponds to the single scenario for kinetic freeze-out, which is not consistent with two or multiple scenarios observed in other studies [63, 64, 65, 66]. We are inclined to use multiple scenarios [67] due to more accurate fit to the wider p_T spectra. To coordinate the single and multiple scenarios, we may regard the multiple scenarios as a refined situation of the single scenario, which will be discussed later in detail.

The trends of excitation functions render that the collision system undergoes different evolution processes. From several GeV to about 10 GeV, the violent degree of collisions increases with increasing the energy and matter density of the collision system. The hadronic matter in the collision system stays at a state with ever higher density and temperature. At about 10 GeV, the energy and matter density of the collision system reaches to a high value. The temperature is also high, which is needed to come into notice. At above 10 GeV, the energy and matter density of the collision system reaches to a higher value. The temperature is also higher. However, because the phase transition from hadronic matter

to QGP had happened possibly, the temperature is limited, which results in the levels of T_0 for pion emission and $\langle T_0 \rangle$ had stabilized.

Before summary and conclusions, we would like to point out that we have used a new method to extract T_0 , β_T , and T_i . After fitting the p_T (m_T) spectra by using the two-component standard distribution Eqs. (6) or (7) in which the free parameters are the effective temperatures T_1 and T_2 and the contribution fraction k of the first component, the derived parameter, the effective temperature T , can be obtained from the weighted average formula Eq. (8). Then, the derived parameters, the kinetic freeze-out temperature T_0 and transverse flow velocity β_T , can be obtained respectively from Eqs. (16) and (17) which are related to the mean transverse momentum $\langle p_T \rangle$. The derived parameter, the initial temperature T_i , can be obtained from Eq. (29) which is related to the root-mean-square $\sqrt{\langle p_T^2 \rangle}$.

According to the analysis of the spectra of six hadron species listed in Tables 1 and 2, one can see that pions, kaons, and (anti)protons correspond to different temperatures of emission source. This shows a mass-dependent multiple scenario for kinetic freeze-out. Moreover, in AA collisions at energies below the LHC, charged pions can be redistributed between two sources, one is hot and another is cold, while kaons and (anti)protons are

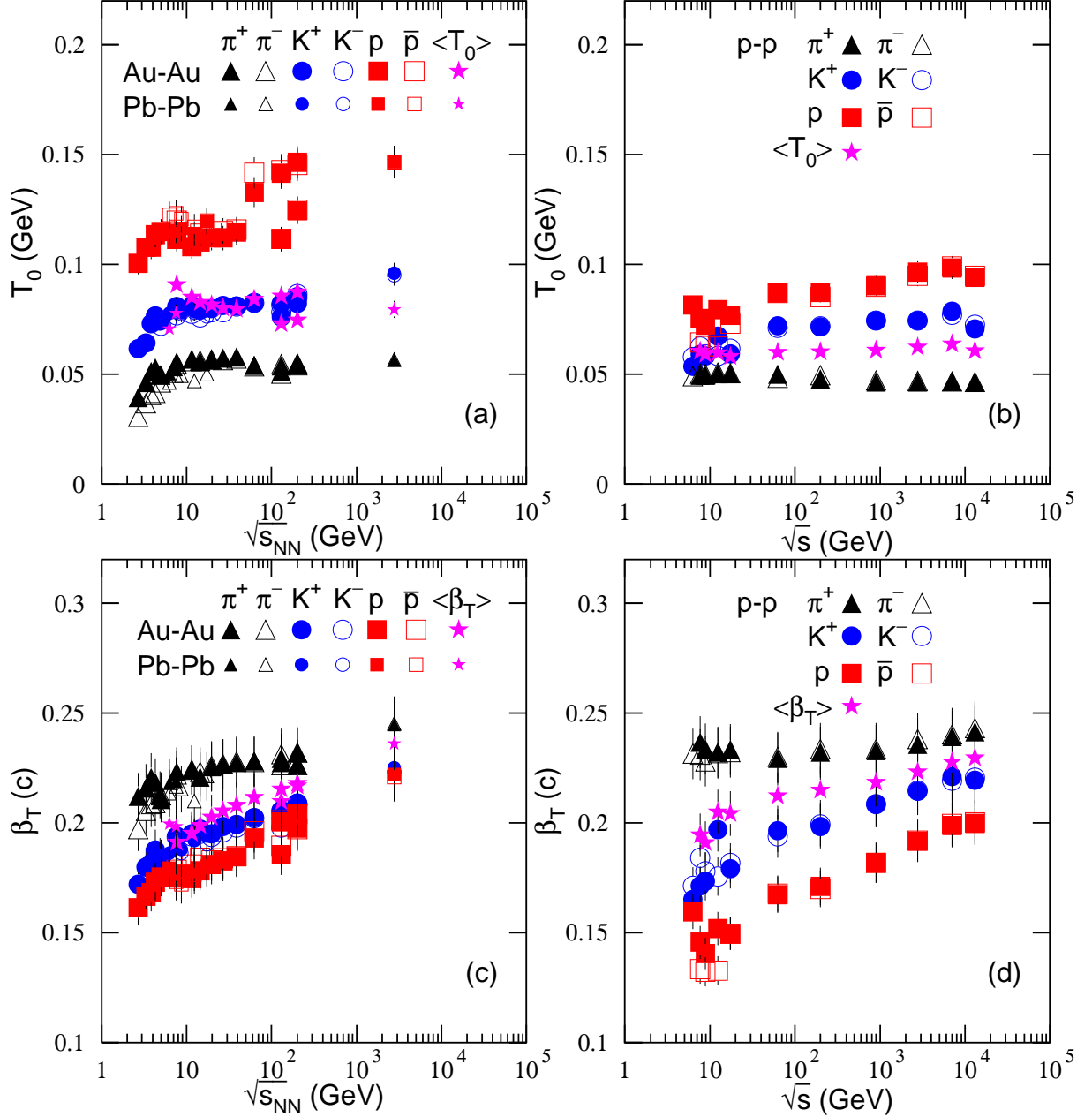


Fig. 5. Same as Fig. 4, but showing the excitation functions of (a)(b) T_0 and $\langle T_0 \rangle$, as well as (c)(d) β_T and $\langle \beta_T \rangle$.

located in single (hot) sources (though with different temperatures) in most cases. This is understandable. That charged pions come from resonance decays contribute a relative large fraction in low- p_T region, which can be described by the first component in Eq. (6) or (7). Some low- p_T pions from non-resonance decay can be also described by the first component. As an ensemble, Eq. (1) describes the cold source with low T for all low- p_T pions. However, the resonance decays for kaons and (anti)protons are relatively small comparing

to those for pions in low- p_T region, which are concealed in single source.

Naturally, if we regard $\langle T \rangle$, $\langle T_0 \rangle$, $\langle \beta_T \rangle$, and $\langle T_i \rangle$ as common quantities corresponding to emissions of various hadron species, we may use the mass-independent single scenario for kinetic freeze-out and other system evolution stages such as chemical freeze-out and initial state. It is contentious that the mass-independent single scenario or mass-dependent multiple scenario is right due to different physics thinkings. In our opinion, the

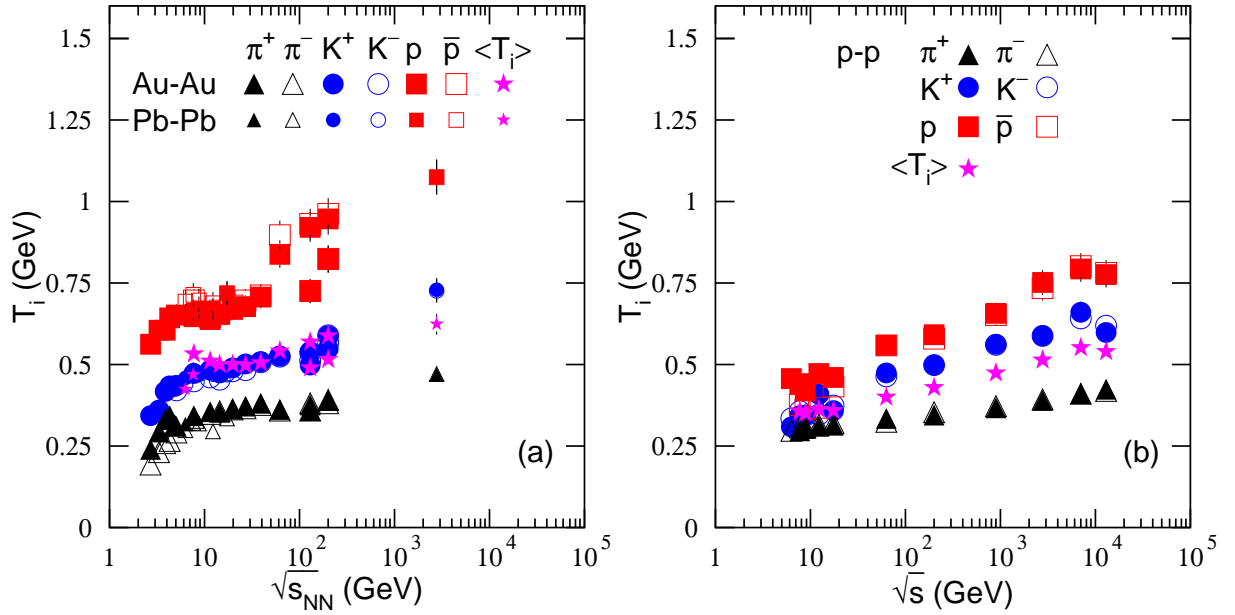


Fig. 6. Same as Fig. 4, but showing the excitation functions of T_i and $\langle T_i \rangle$.

mass-independent single scenario is a very ideal situation which is similar to the equilibrium state of mixture gas. And the mass-dependent multiple scenario describes a refined emission process which “shows massive particles coming out of the system earlier in time with smaller radial flow velocities, which is hydrodynamic behavior” [68]. The temperatures discussed in this paper reflect mainly the kinetic energies of various hadron species, but do not have certainly the statistical sense.

We note that, in the mass-dependent multiple scenario for kinetic freeze-out (Figs. 4 and 5), the obtained temperature for proton emission is much larger than that for pion emission. This reflects that protons coming out of the system is much earlier than pions due to much larger mass of proton comparing to pion. This phenomenon is a hydrodynamic behavior [68], in which massive particles are early leaved behind in the evolution process of collision system. In other words, massive particles are not emitted from the system on their own initiative due to high T_0 , but are leaved behind under compulsion due to low β_T and large m_0 . In fact, some protons existed in projectile and target nuclei appear in rapidity space as leading protons outside the fireball. This issue also results in protons coming out of the system to be earlier than pions.

Because T_0 and β_T are model dependent, this paper is different from Figs. 37 and 39 in ref. [32], though

this paper is less model dependent and ref. [32] is much model dependent. In ref. [32], a flow velocity profile parameter n is used in the extraction of T_0 and β_T . The parameter n can be largely changed from 0 to 2 in AA collisions and above 4 in pp collisions, which is mutable and debatable. The pion spectra in low- p_T region (< 0.5 GeV/c) are excluded from the fit [32] due to resonance decay, which overrates T_0 and β_T . Our work shows that T_0 (β_T) in pp collisions is slightly smaller than (almost equal to) that in AA collisions, which is in agreement with our recent work [12] in which the intercept in the linear relation of T versus m_0 is regarded as T_0 and the slope in the linear relation of $\langle p_T \rangle$ versus $m_0 \bar{\gamma}$ is regarded as β_T . This result is understandable due to similar collective behavior as in AA collisions appearing in pp collisions [10].

We would like to emphasize that this paper is a data-driven reanalysis based on some physics considerations, but not a simple fit to the data. From the data-driven reanalysis, the excitation functions of some quantities such as the effective temperature T and its weighted average $\langle T \rangle$, the kinetic freeze-out temperature T_0 and its weighted average $\langle T_0 \rangle$, the transverse flow velocity β_T and its weighted average $\langle \beta_T \rangle$, as well as the initial temperature T_i and its weighted average $\langle T_i \rangle$ have been obtained. These excitation functions have appeared some obvious laws with the increase of collision energy.

In the above discussions, to obtain $\bar{\gamma}$ then β_T , we

have used the MC method. Figs. 5(c) and 5(d) are a direct result by the MC method. As a statistical model is implemented for Figs. 1–3, we can also obtain the curves by Eq. (19), which is in terms of the MC method. In fact, in the calculation by the MC method, after the shuffled treatment due to the randomness by the Matlab code, we can obtain a lot of “simulated data”. Then, we may count them in different p_T ($m_T - m_0$) bins and obtain similar or the same results to the curves in Figs. 1–3. In the case of the event numbers being not too large, we shall observe fluctuations around the curves. As an example, for K^+ spectra in Figs. 1(a)–1(f), the dotted curves and crosses represent the MC results with high and low statistics respectively. The two results from the analytical function and MC method are confirmed each other.

4 Summary and conclusion

We summarize here our main observations and conclusions.

(a) The transverse momentum or mass spectra of π^+ , π^- , K^+ , K^- , p , and \bar{p} at mid- y or mid- η produced in central Au-Au (Pb-Pb) collisions over an energy range from 2.7 to 200 (6.3 to 2760) GeV have been analyzed in this work. Meanwhile, the spectra in INEL pp collisions over an energy range from 6.3 to 13000 GeV have also been analyzed. In most cases, the experimental data measured by the E866, E895, E802, NA49, NA61/SHINE, STAR, PHENIX, ALICE, and CMS Collaborations are approximately fitted by the (two-component) standard distribution in which the temperature concept is the closest to the ideal gas model.

(b) The effective temperature and its excitation function are obtained from the transverse momentum or mass spectra of identified particles produced in collisions at high energies. The kinetic freeze-out temperature and transverse flow velocity and their excitation functions are extracted from the formulas related to the average transverse momentum, which is based on the multisource thermal model. The initial temperature and its excitation function are extracted from the formula related to the root-mean-square transverse momentum, which is based on the color string percolation model.

(c) With the increase of collision energy, the four derived parameters and each average increase (quickly)

from a few GeV to about 10 GeV, then increases slowly after 10 GeV. In particular, the kinetic freeze-out temperature for pion emission and its average finally appear the trend of saturation at the RHIC and LHC. Meanwhile, the three derived temperatures increases and the derived transverse flow velocity decreases with the increase of particle mass, which result in a mass-dependent multiple scenario for kinetic freeze-out and other system evolution stages such as chemical freeze-out and initial state.

Data Availability

The data used to support the findings of this study are included within the article and are cited at relevant places within the text as references.

Ethical Approval

The authors declare that they are in compliance with ethical standards regarding the content of this paper.

Disclosure

The funding agencies have no role in the design of the study; in the collection, analysis, or interpretation of the data; in the writing of the manuscript; or in the decision to publish the results.

Conflicts of Interest

The authors declare that there are no conflicts of interest regarding the publication of this paper.

Acknowledgments

This work was supported by the National Natural Science Foundation of China under Grant Nos. 11575103 and 11947418, the Chinese Government Scholarship (China Scholarship Council), the Scientific and Technological Innovation Programs of Higher Education Institutions in Shanxi (STIP) under Grant No. 201802017, the Shanxi Provincial Natural Science Foundation under Grant No. 201901D111043, and the Fund for Shanxi “1331 Project” Key Subjects Construction.

References

- [1] S. Gupta, X. F. Luo, B. Mohanty, H. G. Ritter, and N. Xu, “Scale for the phase diagram of quantum chromodynamics,” *Science*, vol. 332, pp. 1525–1528, 2011.
- [2] N. Xu for the STAR Collaboration, “An overview of STAR experimental results,” *Nuclear Physics A*, vol. 931, pp. 1–12, 2014.

- [3] A. Andronic, P. Braun-Munzinger, K. Redlich, and J. Stachel, “Decoding the phase structure of QCD via particle production at high energy,” *Nature*, vol. 561, pp. 321–330, 2018.
- [4] STAR Collaboration, J. Adams et al., “Experimental and theoretical challenges in the search for the quark gluon plasma: The STAR Collaboration’s critical assessment of the evidence from RHIC collisions,” *Nuclear Physics A*, vol. 757, pp. 102–183, 2005.
- [5] PHENIX Collaboration, K. Adcox et al., “Formation of dense partonic matter in relativistic nucleus-nucleus collisions at RHIC: Experimental evaluation by the PHENIX collaboration,” *Nuclear Physics A*, vol. 757, pp. 184–283, 2005.
- [6] J. F. Grosse-Oetringhaus for the ALICE Collaboration, “Overview of ALICE results at Quark Matter 2014,” *Nuclear Physics A*, vol. 931, pp. 22–31, 2014.
- [7] X.F. Luo and N. Xu, “Search for the QCD critical point with fluctuations of conserved quantities in relativistic heavy-ion collisions at RHIC: an overview,” *Nuclear Science and Techniques*, vol. 28, article 112, 2017.
- [8] M. R. Haque, C. Jena, and B. Mohanty, “A review of elliptic flow of light nuclei in heavy-ion collisions at RHIC and LHC energies,” *Advances in High Energy Physics*, vol. 2018, Article ID 1248563, 2018.
- [9] S. Bhattacharyya, M. Haiduc, A. T. Neagu, and E. Firtu, “A comparative study of K^\pm/π^\pm ratio in proton-proton collisions at different energies: Experimental results versus model simulation,” *Advances in High Energy Physics*, vol. 2018, Article ID 6307205, 2018.
- [10] H. C. Song, Y. Zhou, and K. Gajdošová, “Collective flow and hydrodynamics in large and small systems at the LHC,” *Nuclear Science and Techniques*, vol. 28, article 99, 2017.
- [11] S. Schlichting and P. Tribedy, “Collectivity in small collision systems: An initial-state perspective,” *Advances in High Energy Physics*, vol. 2016, Article ID 8460349, 2016.
- [12] H.-L. Lao, F.-H. Liu, B.-C. Li, M.-Y. Duan, and R. A. Lacey, “Examining the model dependence of the determination of kinetic freeze-out temperature and transverse flow velocity in small collision system,” *Nuclear Science and Techniques*, vol. 29, article 164, 2018.
- [13] H.-L. Lao, F.-H. Liu, B.-C. Li, and M.-Y. Duan, “Kinetic freeze-out temperatures in central and peripheral collisions: which one is larger?,” *Nuclear Science and Techniques*, vol. 29, article 82, 2018.
- [14] J. Cleymans, “The physics case for the $\sqrt{s_{NN}} \approx 10$ GeV energy region,” in *Walter Greiner Memorial Volume*, edited by P. O. Hess (World Scientific, Singapore) 2018) [arXiv:1711.02882 [hep-ph]]
- [15] A. Andronic, P. Braun-Munzinger, and J. Stachel, “Thermal hadron production in relativistic nuclear collisions,” *Acta Physica Polonica B*, vol. 40, pp. 1005–1012, 2009.
- [16] A. Andronic, P. Braun-Munzinger, and J. Stachel, “The horn, the hadron mass spectrum and the QCD phase diagram: The statistical model of hadron production in central nucleus-nucleus collisions,” *Nuclear Physics A*, vol. 834, pp. 237c–240c, 2010.
- [17] J. Cleymans, H. Oeschler, K. Redlich, and S. Wheaton, “Comparison of chemical freeze-out criteria in heavy-ion collisions,” *Physical Review C*, vol. 73, Article ID 034905, 2006.
- [18] A. Andronic, P. Braun-Munzinger, and J. Stachel, “Hadron production in central nucleus-nucleus collisions at chemical freeze-out,” *Nuclear Physics A*, vol. 772, pp. 167–199, 2006.
- [19] F.-H. Liu, Y.-Q. Gao, T. Tian, and B.-C. Li, “Unified description of transverse momentum spectrums contributed by soft and hard processes in high-energy nuclear collisions,” *The European Physical Journal A*, vol. 50, article 94, 2014.
- [20] L.-N. Gao, F.-H. Liu, and R. A. Lacey, “Excitation functions of parameters in Erlang distribution, Schwinger mechanism, and Tsallis statistics in RHIC BES program,” *The European Physical Journal A*, vol. 52, article 137, 2016.
- [21] W.-J. Xie, “Transverse momentum spectra in high-energy nucleus-nucleus, proton-nucleus and proton-proton collisions,” *Chinese Physics C*, vol. 35, pp. 1111–1119, 2011.
- [22] L. J. Gutay, A. S. Hirsch, C. Pajares, R. P. Scharenberg, and B. K. Srivastava, “De-confinement in small systems: Clustering of color sources in high multiplicity $\bar{p}p$ collisions at $\sqrt{s} = 1.8$ TeV,” *International Journal of Modern Physics E*, vol. 24, article 1550101, 2015.
- [23] A. S. Hirsch, C. Pajares, R. P. Scharenberg, and B. K. Srivastava, “Exploring the initial stage of high multiplicity proton-proton collisions by determining the initial temperature of the quark-gluon plasma,” *Physical Review D*, vol. 100, Article ID 114040, 2019.
- [24] P. Sahoo, S. De, S. K. Tiwari, and R. Sahoo, “Energy and centrality dependent study of deconfinement phase transition in a color string percolation approach at RHIC energies,” *The European Physical Journal A*, vol. 54, article 136, 2018.
- [25] E866 Collaboration, L. Ahle et al., “Excitation function of K^+ and π^+ production in Au+Au reactions at 2–10A GeV,” *Physics Letters B*, vol. 476, pp. 1–8, 2000.
- [26] E895 Collaboration, J. L. Klay et al., “Longitudinal flow from 2–8A GeV Au+Au collisions at the Brookhaven AGS,” *Physical Review Letters*, vol. 88, Article ID 102301, 2002.

- [27] E895 Collaboration, J. L. Klay et al., “Charged pion production in 2–8A GeV central Au+Au Collisions,” *Physical Review C*, vol. 68, Article ID 054905, 2003.
- [28] E802 Collaboration, L. Ahle et al., “Kaon production in Au+Au collisions at 11.6A GeV/c,” *Physical Review C*, vol. 58, pp. 3523–3538, 1998.
- [29] E802 Collaboration, L. Ahle et al., “Particle production at high baryon density in central Au+Au reactions at 11.6A GeV/c,” *Physical Review C*, vol. 57, pp. R466–R470, 1998.
- [30] STAR Collaboration, L. Aamczyk et al., “Bulk properties of the medium produced in relativistic heavy-ion collisions from the beam energy scan program,” *Physical Review C*, vol. 96, Article ID 044904, 2017.
- [31] V. Bairathi for the STAR Collaboration, “Study of the bulk properties of the system formed in Au+Au collisions at $\sqrt{s_{NN}} = 14.5$ GeV using the STAR detector at RHIC,” *Nuclear Physics A*, vol. 956, pp. 292–295, 2018.
- [32] STAR Collaboration, B. I. Abelev et al., “Systematic measurements of identified particle spectra in pp , d +Au, and Au+Au collisions at the STAR detector,” *Physical Review C*, vol. 79, Article ID 034909, 2009.
- [33] PHENIX Collaboration, K. Adcox et al., “Centrality dependence of π^+/π^- , K^+/K^- , p and \bar{p} production from $\sqrt{s_{NN}} = 13$ GeV Au+Au collisions at RHIC,” *Physical Review Letters*, vol. 88, Article ID 242301, 2002.
- [34] PHENIX Collaboration, S. S. Adler et al., “Identified charged particle spectra and yields in Au+Au collisions at $\sqrt{s_{NN}} = 200$ GeV,” *Physical Review C*, vol. 69, Article ID 034909, 2004.
- [35] NA49 Collaboration, C. Alt et al., “Energy and centrality dependence of \bar{p} and p production and the $\bar{\Lambda}/\bar{p}$ ratio in Pb+Pb collisions between 20A GeV and 158A GeV,” *Physical Review C*, vol. 73, Article ID 044910, 2006.
- [36] NA49 Collaboration, C. Alt et al., “Pion and kaon production in central Pb+Pb collisions at 20A and 30A GeV: Evidence for the onset of deconfinement,” *Physical Review C*, vol. 77, Article ID 024903, 2008.
- [37] NA49 Collaboration, S. V. Afanasiev et al., “Energy dependence of pion and kaon production in central Pb+Pb collisions,” *Physical Review C*, vol. 66, Article ID 054902, 2002.
- [38] ALICE Collaboration, B. Abelev et al., “Centrality dependence of π , K , and p production in Pb-Pb collisions at $\sqrt{s_{NN}} = 2.76$ TeV,” *Physical Review C*, vol. 88, Article ID 044910, 2013.
- [39] NA61/SHINE Collaboration, N. Abgrall et al., “Measurement of negatively charged pion spectra in inelastic $p + p$ interactions at $p_{lab} = 20, 31, 40, 80$ and 158 GeV/c,” *The European Physical Journal C*, vol. 74, article 2794, 2014.
- [40] NA61/SHINE Collaboration, A. Aduszkiewicz et al., “Measurements of π^\pm , K^\pm , p and \bar{p} spectra in proton-proton interactions at 20, 31, 40, 80 and 158 GeV/c with the NA61/SHINE spectrometer at the CERN SPS,” *The European Physical Journal C*, vol. 77, article 671, 2017.
- [41] PHENIX Collaboration, A. Adare et al., “Identified charged hadron production in $p+p$ collisions at $\sqrt{s} = 200$ and 62.4 GeV,” *Physical Review C*, vol. 83, Article ID 064903, 2011.
- [42] CMS Collaboration, S. Chatrchyan et al., “Study of the inclusive production of charged pions, kaons, and protons in pp collisions at $\sqrt{s} = 0.9, 2.76$, and 7 TeV,” *The European Physical Journal C*, vol. 72, article 2164, 2012.
- [43] CMS Collaboration, A. M. Sirunyan et al., “Measurement of charged pion, kaon, and proton production in proton-proton collisions at $\sqrt{s} = 13$ TeV,” *Physical Review D*, vol. 96, Article ID 112003, 2017.
- [44] J. Cleymans and D. Worku, “Relativistic thermodynamics: Transverse momentum distributions in high-energy physics,” *The European Physical Journal A*, vol. 48, article 160, 2012.
- [45] C. Tsallis, “Possible generalization of Boltzmann-Gibbs statistics,” *Journal of Statistical Physics*, vol. 52, pp. 479–487, 1988.
- [46] T. S. Biró, G. Purcsel, and K. Ürmösy, “Non-extensive approach to quark matter,” *The European Physical Journal A*, vol. 40, article 325, 2009.
- [47] H. Zheng and L. L. Zhu, “Comparing the Tsallis distribution with and without thermodynamical description in $p+p$ Collisions,” *Advances in High Energy Physics*, vol. 2016, Article ID 9632126, 2016.
- [48] J. Schwinger, “On gauge invariance and vacuum polarization,” *Physical Review*, vol. 82, pp. 664–679, 1951.
- [49] R.-C. Wang and C.-Y. Wong, “Finite-size effect in the Schwinger particle-production mechanism,” *Physical Review D*, vol. 38, pp. 348–359, 1988.
- [50] C.-Y. Wong, *Introduction to High Energy Heavy Ion Collisions* (World Scientific, Singapore), 1994.
- [51] P. Braun-Munzinger, K. Redlich, and J. Stachel, “Particle production in heavy ion collisions,” in *Quark-Gluon Plasma 3*, edited by R. C. Hwa and X.-N. Wang (World Scientific, Singapore), 2004 [arXiv:nucl-th/0304013].
- [52] E. Schnedermann, J. Sollfrank, and U. Heinz, “Thermal phenomenology of hadrons from 200A GeV S+S collisions,” *Physical Review C*, vol. 48, pp. 2462–2475, 1993.
- [53] B. I. Abelev et al (STAR Collaboration), “Identified particle production, azimuthal anisotropy, and interferometry measurements in Au+Au collisions at $\sqrt{s_{NN}} = 9.2$ GeV,” *Physical Review C*, vol. 81, Article ID 024911, 2010.

- [54] Z. B. Tang, Y. C. Xu, L. J. Ruan, G. van Buren, F. Q. Wang, and Z. B. Xu, “Spectra and radial flow in relativistic heavy ion collisions with Tsallis statistics in a blast-wave description,” *Physical Review C*, vol. 79, Article ID 051901(R), 2009.
- [55] Z. B. Tang, L. Yi, L. J. Ruan, M. Shao, H. F. Chen, C. Li, B. Mohanty, P. Sorensen, A. H. Tang, and Z. B. Xu, “Statistical origin of constituent-quark scaling in the QGP hadronization,” *Chinese Physics Letters*, vol. 30, article 031201, 2013.
- [56] K. Jiang, Y. Y. Zhu, W. T. Liu, H. F. Chen, C. Li, L. J. Ruan, Z. B. Tang, and Z. B. Xu, “Onset of radial flow in $p+p$ collisions,” *Physical Review C*, vol. 91, Article ID 024910, 2015.
- [57] R. Hagedorn, “Multiplicities, p_T distributions and the expected hadron \rightarrow quark-gluon phase transition,” *Rivista del Nuovo Cimento*, vol. 6, no. 10, pp. 1–50, 1983.
- [58] P. Koch, J. Rafelski, and W. Greiner, “Strange hadron in hot nuclear matter,” *Physics Letters B*, vol. 123, pp. 151–154, 1983.
- [59] P. Braun-Munzinger, D. Magestro, K. Redlich, and J. Stachel, “Hadron production in Au-Au collisions at RHIC,” *Physics Letters B*, vol. 518, pp. 41–46, 2001.
- [60] J.-Y. Ollitrault, “Revealing QCD thermodynamics in ultra-relativistic nuclear collisions,” Proc. 28th Int. Conf. Ultrarelativistic Nucleus-Nucleus Collisions (Quark Matter 2019), Wuhan, China, 4–9 Nov. 2019, *Nuclear Physics A*, to appear, 2020.
- [61] Y.-H. Chen and F.-H. Liu, “Event patterns extracted from anisotropic spectra of charged particles produced in Pb-Pb collisions at 2.76 TeV,” *The European Physical Journal A*, vol. 53, article 230, 2017.
- [62] H.-X. Zhang and P.-J. Shan, “Statistical simulation method for determining the errors of fit parameters,” Proc. 8th Natl. Conf. Nucl. Phys. (the next volume), Xi’an, China, 3–7 Dec. 1991 [<http://cpfd.cnki.com.cn/Article/CPFDTOTAL-HWLX19911200>] (in Chinese).
- [63] S. Chatterjee, S. Das, L. Kumar, D. Mishra, B. Mohanty, R. Sahoo, and N. Sharma, “Freeze-out parameters in heavy-ion collisions at AGS, SPS, RHIC, and LHC energies,” *Advances in High Energy Physics*, vol. 2015, Article ID 349013, 2015.
- [64] S. Chatterjee, B. Mohanty, and R. Singh, “Freezeout hypersurface at energies available at the CERN Large Hadron Collider from particle spectra: Flavor and centrality dependence,” *Physical Review C*, vol. 92, Article ID 024917, 2015.
- [65] S. Chatterjee and B. Mohanty, “Production of light nuclei in heavy-ion collisions within a multiple-freezeout scenario,” *Physical Review C*, vol. 90, Article ID 034908, 2014.
- [66] D. Thakur, S. Tripathy, P. Garg, R. Sahoo, and J. Cleymans, “Indication of a differential freeze-out in proton-proton and heavy-ion collisions at RHIC and LHC energies,” *Advances in High Energy Physics*, vol. 2016, Article ID 4149352, 2016.
- [67] H.-L. Lao, H.-R. Wei, F.-H. Liu, and R. A. Lacey, “An evidence of mass-dependent differential kinetic freeze-out scenario observed in Pb-Pb collisions at 2.76 TeV,” *The European Physical Journal A*, vol. 52, article 203, 2016.
- [68] R. Sahoo, “Possible formation of QGP-droplets in proton-proton collisions at the CERN Large Hadron Collider,” *AAPPS Bulletin*, vol. 29, no. 4, pp. 16–21, 2019.